國立臺灣大學理學院物理學研究所

碩士論文

Department of Physics

College of Science

National Taiwan University

Master’s Thesis

利用定向電場增強二維材料邊緣的電化學活性

Enhancing the Electrochemical Activity of 2D Materials Edges through Oriented Electric Fields

汪灝

Hao Wang

指導教授：謝馬利歐 博士

Advisor: Mario Hofmann, Ph.D.

中華民國 113 年 7 月

July 2024

doi:10.6342/NTU202402275

Acknowledgement

I would like to express my sincere gratitude to all those who have supported and contributed to the completion of this thesis.

First and foremost, I would like to thank my advisors, Prof. Ya-Ping Hsieh and Prof. Mario Hofmann for their invaluable guidance, encouragement, and patience throughout the entire process. Their insights and expertise have greatly influenced the direction and quality of this work.

I am also grateful to the members of my thesis committee, Prof. Yang-Fang Chen, and Prof. Chen-Hao Wang for their constructive feedback and support.

A special thanks to my family and friends for their unwavering support and encouragement. Their belief in me has been a constant source of motivation.

I would also like to acknowledge my colleagues and peers for their camaraderie and for creating an inspiring and collaborative environment. Special thanks to Ding-Rui for providing a lot of data and help. I am very fortunate to have many good comrades in MY lab, whether it is experimental or moral support. I enjoy spending time with you guys. Thank you for accompanying me through these years of journey.

This thesis would not have been possible without the collective efforts and support of all these individuals. Thank you.

doi:10.6342/NTU202402275

摘要

二维材料邊緣作為電化學催化系統具有廣闊的前景，但其催化性能仍然不及貴金屬。我們展示了利用定向電場(OEFs)增強二维材料邊緣電化學活性的潛力。通過原子級別的工程設計，我們在氟化石墨烯/石墨烯/二硫化鉬異質結構(fluorographene/graphene/MoS_2 heterojunction)的邊緣產生了強力且局部化的電場，並通過模擬和空間分辨光譜進行表徵。邊緣定向外部電場的獨特靜電特性顯著提高了邊緣與電解質之間的異質電荷傳輸速率，達到了兩個數量級的提升，這一點通過阻抗光譜(EIS)得到了驗證。第一性原理計算表明，這一改進源於電場誘導的反應物吸附能降低。我們將這種定向電場增強的邊緣反應應用於氫氣析出反應(HER)，並觀察到極佳的電催化效果，這體現在塔菲爾斜率降低了 30%，以及 2D 材料達到了前所未有的轉換頻率(turnover frequency)。我們的發現為未來複雜反應中調整 2D 材料的催化特性開闢了一條新途徑。

關鍵字：二維材料、二維邊緣、電化學、定向電場、析氫反應

ABSTRACT

Two-dimensional (2D) material edges have shown promise as electrochemical catalysts, but their performance has not yet matched that of noble metals. In this study, we explore the use of oriented electric fields (OEFs) to boost the electrochemical activity of 2D material edges. We engineered the edge of a fluorographene/graphene/MoS_2 heterojunction nanoribbon at the atomic level, creating powerful and localized OEFs. These fields were analyzed using simulations and spatially-resolved spectroscopy. The unique electrostatic properties of the fringing OEF led to a hundredfold increase in the heterogeneous charge transfer rate between the edge and the electrolyte, as shown by impedance spectroscopy. Ab-initio calculations suggest that this improvement stems from a field-induced reduction in reactant adsorption energy. We applied this OEF-enhanced edge reactivity to hydrogen evolution reactions (HER), achieving exceptional electrochemical performance. This was evidenced by a 30% decrease in Tafel slope and a record-breaking turnover frequency for 2D materials. Our research paves the way for fine-tuning the catalytic properties of 2D materials for future complex reactions.

Keywords: 2D materials, 2D edges, electrochemistry, oriented electric fields, HER

doi:10.6342/NTU202402275

CONTENTS

doi:10.6342/NTU202402275

doi:10.6342/NTU202402275

LIST OF FIGURES

doi:10.6342/NTU202402275

doi:10.6342/NTU202402275

Chapter 1 Introduction

1.1 Two-dimensional (2D) materials

Two-dimensional (2D) materials are an extraordinary class of materials characterized by their atomically thin structure, consisting of a single or few layers of atoms arranged in a planar configuration. The discovery of graphene, a single layer of carbon atoms, by Andre Geim and Konstantin Novoselov in 2004 sparked a revolution in the exploration of 2D materials[1]. Since then, a diverse family of 2D materials has emerged (**Figure 1.1-1**), including transition metal dichalcogenides (TMDCs, e.g., MoS_2, WS_2)[2-4], hexagonal boron nitride (h-BN)[5], transition metal oxides (TMOs, e.g., MoO_3)[6, 7], and transition metal carbides/nitrides (MXenes, e.g., Ti_2C, Ti_3CN)[8-10]. These materials exhibit remarkable electronic, optical, mechanical, and thermal properties that diverge significantly from their bulk counterparts due to their ultra-thin nature and quantum confinement effects. The exploration of novel 2D materials and the understanding of their fundamental physics continue to drive scientific curiosity and technological innovation, positioning 2D materials as a promising avenue for

doi:10.6342/NTU202402275

transformative technologies across various industries.

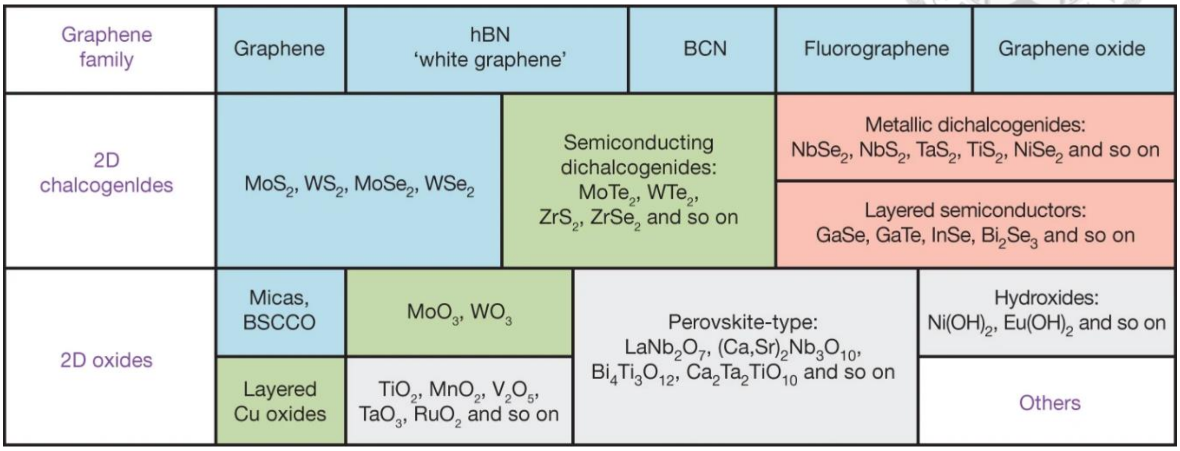

Graphene family	Graphene	hBN 'white graphene'	BCN	Fluorographene	Graphene oxide
2D chalcogenides	MoS_2, WS_2, $MoSe_2$, WSe_2		Semiconducting dichalcogenides: $MoTe_2$, WTe_2, ZrS_2, $ZrSe_2$ and so on	Metallic dichalcogenides: $NbSe_2$, NbS_2, TaS_2, TiS_2, $NiSe_2$ and so on Layered semiconductors: GaSe, GaTe, InSe, Bi_2Se_3 and so on	
2D oxides	Micas, BSCCO	MoO_3, WO_3	Perovskite-type: $LaNb_2O_7$, $(Ca,Sr)_2Nb_3O_{10}$, $Bi_4Ti_3O_{12}$, $Ca_2Ta_2TiO_{10}$ and so on	Hydroxides: $Ni(OH)_2$, $Eu(OH)_2$ and so on	
	Layered Cu oxides	TiO_2, MnO_2, V_2O_5, TaO_3, RuO_2 and so on		Others	

Figure 1.1-1 2D materials family [11]

[redacted]Graphene

Graphene is a two-dimensional structure formed by a single layer of carbon atoms tightly packed in a hexagonal honeycomb lattice with sp^2 hybridized orbitals, having a thickness of only a single atomic layer (0.3–0.5 nm), making it one of the thinnest and hardest materials. Graphene exhibits significantly different properties from graphite **(Figure 1.1-2)**, possessing a high theoretical surface area (2630 m^2g^{-1}), superior electrical conductivity and carrier mobility (200000 $cm^2\ V^{-1}\ s^{-1}$)[12], Young's modulus (~1.0 TPa)[13], thermal conductivity (~5000 $Wm^{-1}K^{-1}$)[14], and optical transparency (~97.7%)[15]. The unique properties of graphene arise from its two-dimensional geometry and the nature of its constituent carbon atoms, making it an attractive material for various applications, including electronics[16], optoelectronics[17], energy storage[18], and sensing[19].

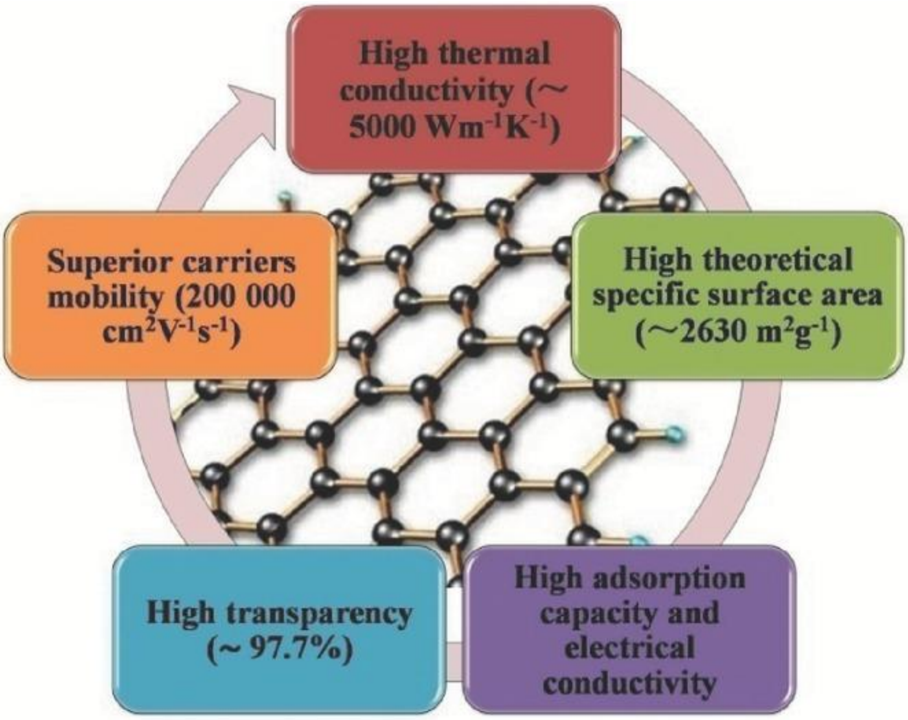

Figure 1.1-2 The superior properties of pristine graphene.[20]

[redacted]Fluorinated graphene

Graphene, despite its notable advantages, has several limitations, including structural imperfections, low chemical reactivity, and a zero bandgap. To address these issues and enhance graphene's properties, researchers have employed various modification techniques. These methods involve attaching chemical compounds, introducing functional groups, or creating free radicals on graphene or its related materials. Such modifications aim to strengthen the material's structure, increase its surface reactivity, and improve its processing ability for practical applications.[21-24]

Fluorinated graphene (fluorographene) is a typical member of functionalized graphene, which has thousands of halogen atoms on graphene with the transition of carbon atoms from sp^2 to sp^3 hybridization. It combines a two-dimensional structure, wide bandgap, and high stability, making it an attractive material for various applications due to its unique carbon-fluorine (C-F) bonds.

There are two primary methods for synthesizing fluorinated graphene: fluorination and exfoliation. Fluorination involves direct gas-fluorination[25], plasma fluorination[26, 27], hydrothermal fluorination[28], and photochemical/electrochemical synthesis[29, 30]. Exfoliation methods involve sonochemical techniques, modified Hummer’s exfoliation[31], and thermal exfoliation[32]. The type and amount of C-F bonds (covalent, semi-ionic, and ionic) influence its properties, such as bandgap, thermal and chemical stability, dispersibility, semiconducting nature, and mechanical properties.
The calculation shows an increase in the fluorine-to-carbon (F/C) ratio expands the bandgap **(Figure 1.1-3)**, while a lower F/C ratio supports charge transport based on π-conjugated structures. The formation of sp^3 bonds resulted in significant in charge

doi:10.6342/NTU202402275

densities and scattering centers within the conduction band.[33]

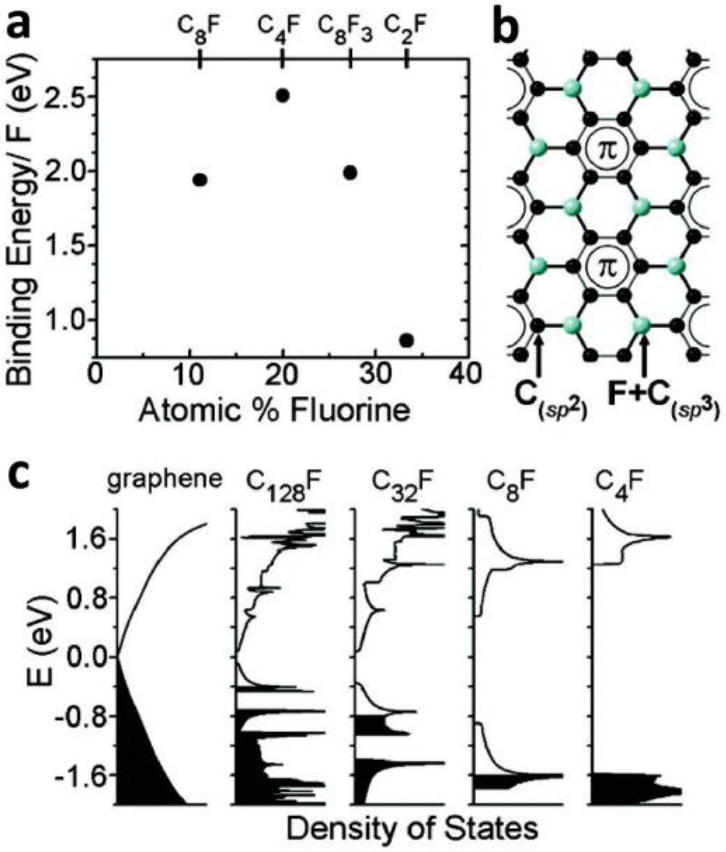

Figure 1.1-3 (a) Calculated binding energy per F atom compared to the F_2 gas state. (b) Sketch of the calculated C_4F configuration for the 25% coverage from (a). (c) Calculated total DOS of single-side fluorinated graphene.[33]

Additionally, in our previous report[34], we revealed the exceptional precision at the atomic level in fluorographene's reactivity, which has led to the development of a new multi-patterning technique. We observed a significant difference in behavior between single-layer and bilayer graphene when exposed to a CF_4 plasma in a glow-discharge state. Single-layer graphene is completely removed by the plasma, while bilayer graphene shows indefinite resistance to it. This remarkable chemical selectivity is explained by a mutual stabilization effect. The top layer becomes fluorinated, the bottom layer remains in its original state (**Figure 1.1-4a**), and these layers interact through van der Waals forces, creating a protective effect. This result is proved by the Optical image, Raman spectrum, and TEM image (**Figure 1.1-4b, 4c, and 4d, more details in section 3.1**). The highly localized nature of this phenomenon allows for extremely sharp transitions at the atomic scale along the lateral plane. This property makes fluorographene an excellent candidate for creating highly precise etch masks, which can be applied to a wide range of substrate materials. This discovery opens up new possibilities for nanoscale fabrication and material processing techniques.

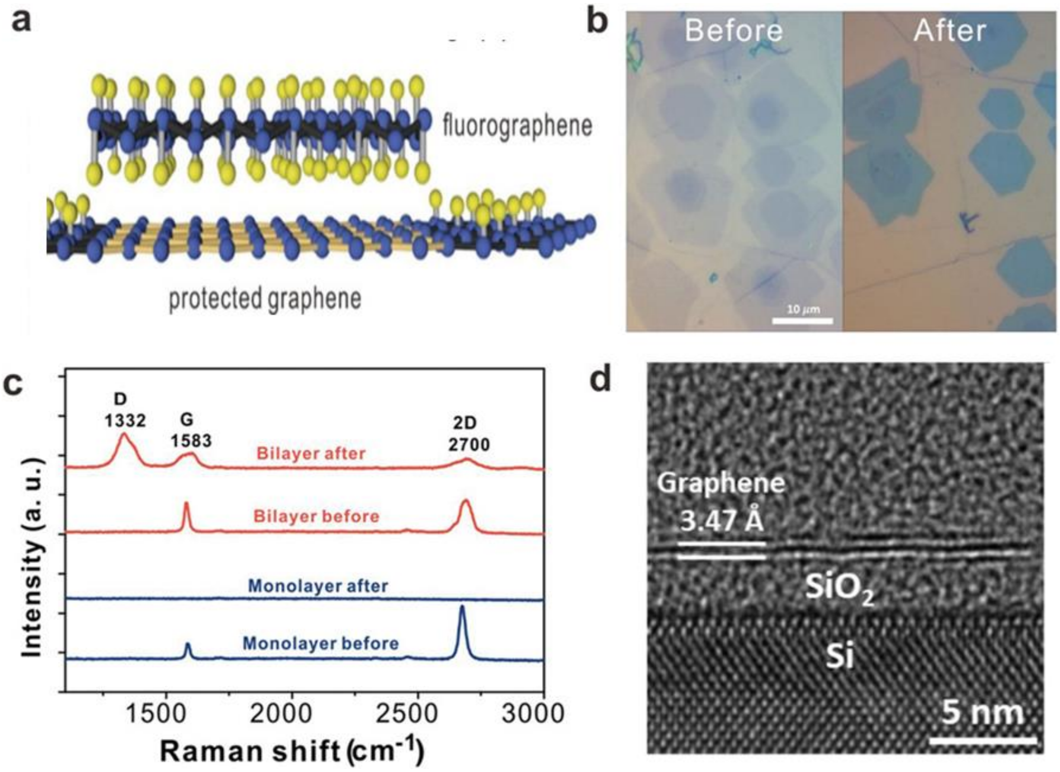

Figure 1.1-4 (a) Schematic of the bilayer transformation after plasma treatment (b) Optical micrographs of graphene before and after CF_4 plasma treatment. (c) Raman spectra derived from monolayer and bilayer graphene before and after plasma treatment (d) Cross-sectional TEM image of the remaining graphene area after 10 min plasma exposure.[34]

[redacted]Transition metal dichalcogenides (TMDs)

Transition metal dichalcogenides (TMDs) is one group of 2D materials which structured in layers, with each layer consisting of a transition metal (M) sandwiched between two layers of chalcogen atoms (X), forming an MX_2 unit (**Figure1.1-5a**). The atomic arrangement in 2D TMDs can be classified into three main structural categories: trigonal prismatic (hexagonal or H-phase), octahedral (tetragonal or T-phase), and a distorted variant of the octahedral structure (T′-phase) (**Figure1.1-5b**).

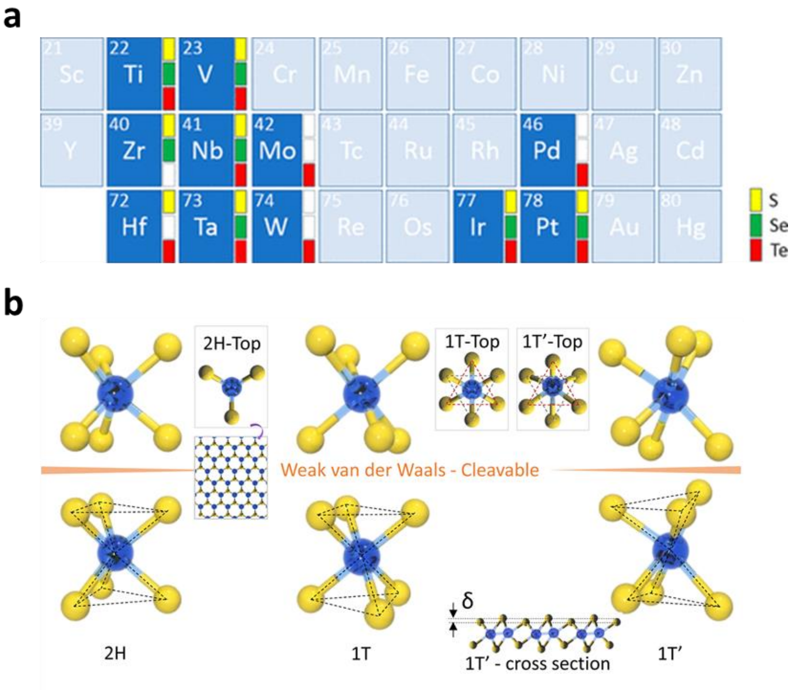

Figure 1.1-5 (a) Types of metals involved in layered dichalcogenides. Blue color indicates transition metals for currently developed metallic-layered dichalcogenides, and yellow, green, and red small rectangles are S, Se, and Te compounds. White rectangles for chalcogen are unreported or nonexist phases.[35] (b) Typical structures of TMDs (2H, 1T, 1T’).[36]

Figure 1.1-6a provides a comprehensive overview of the various TMDs, detailing their structural characteristics and associated properties. These properties include phenomena such as charge density waves (CDW), magnetic behaviors (both ferromagnetic and anti-ferromagnetic), and superconductivity. Also, TMDs exhibit a broad spectrum of bandgaps spanning the entire visible and infrared range, depending on the specific material chosen[37]. The majority of semiconducting TMDs display a direct bandgap in their monolayer form, while their bulk counterparts typically have an indirect bandgap. Notable exceptions to this trend are GaSe and ReS_2, which maintain a direct bandgap even in bulk form[38, 39]. Several monolayer dichalcogenides, including MoS_2, $MoSe_2$, (2H)-$MoTe_2$, WS_2, and WSe_2, demonstrate direct bandgaps ranging from 1.1 eV to 2.1 eV (**Figure 1.1-6b**). In contrast, the bulk forms of these materials typically exhibit indirect bandgaps with lower energy values. Therefore, most MX_2 compounds can exist in both metallic and semiconducting phases, adding to their versatility and potential applications.

doi:10.6342/NTU202402275

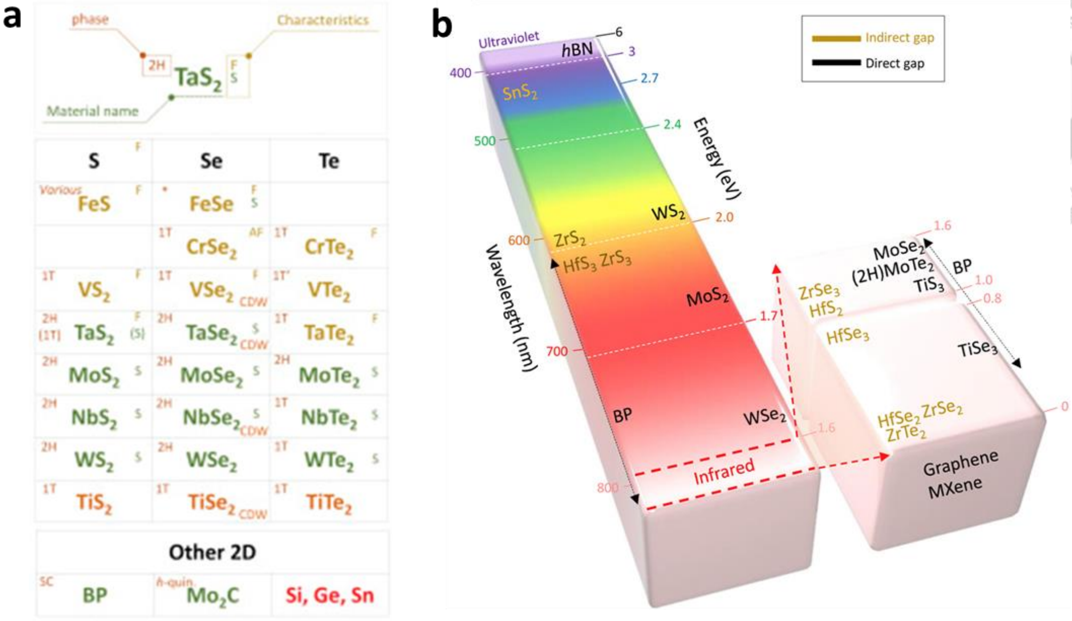

S	Se	Te
Various FeS F	• FeSe F S	
	1T CrSe2 AF	1T CrTe2 F
1T VS2 F	1T VSe2 F CDW	1T' VTe2
2H (1T) TaS2 F (S)	2H TaSe2 S CDW	1T TaTe2 F
2H MoS2 S	2H MoSe2 S	2H MoTe2 S
2H NbS2 S	2H NbSe2 S CDW	1T NbTe2 S
2H WS2 S	2H WSe2	1T WTe2 S
1T TiS2	1T TiSe2 CDW	1T TiTe2
Other 2D		
SC BP	h-quin. Mo2C	Si, Ge, Sn

Figure 1.1-6 (a) Table for various 2D TMDs exhibiting various physical properties such as ferromagnetic (F)/anti-ferromagnetic (AF), superconductivity (s), charge density wave (CDW), and crystal structures (2H, 1T). (b) Bandgap of 2D layered materials varies from zero band gap of graphene (white color) to wide bandgap of h-BN. The color in the column presents the corresponding wavelength of bandgap, [36]

Many MX_2 compounds are characterized by the absence of dangling bonds, and some exhibit high mobility. However, this mobility can be influenced by factors such as the choice of substrate, metal contacts, and the presence of grain boundaries. MoS_2, for instance, demonstrates varying mobility depending on its environment. On SiO_2/Si substrate with scandium (Sc) contact, it can reach 700 $cm^2\ V^{-1}\ s^{-1}$ [40], while on BN/Si substrate at room temperature, it ranges from 33 to 151 $cm^2\ V^{-1}\ s^{-1}$ [41].

In addition to their electrical properties, TMDs share mechanical characteristics with graphene, being both flexible and strong. Suspended few-layer MoS_2 nanosheets have shown a remarkably high Young's modulus of approximately 0.33 ± 0.07 TPa [42]. For single-layer MoS_2, Bertolazzi et al. [43] reported an in-plane stiffness of about 180 ± 60 $N\ m^{-1}$ and a Young's modulus of roughly 270 ± 100 GPa. These superior mechanical properties are attributed to the atomically thin TMDs' lack of stacking faults, high crystallinity, and defect-free nature.

[redacted]Heterostructures

The two-dimensional geometry of these materials not only offers a high surface-to-volume ratio but also allows for the precise engineering of their properties through various techniques, such as doping, strain engineering, and the creation of heterostructures by stacking different 2D materials (**Figure 1.1-7**)[11, 44]. By stacking different 2D materials on top of each other, 2D heterostructures offer a highly customizable platform for creating advanced materials with tailored electronic properties, enhanced charge carrier mobility, and versatile functionality, making them a focal point of research in materials science and nanotechnology [45].

doi:10.6342/NTU202402275

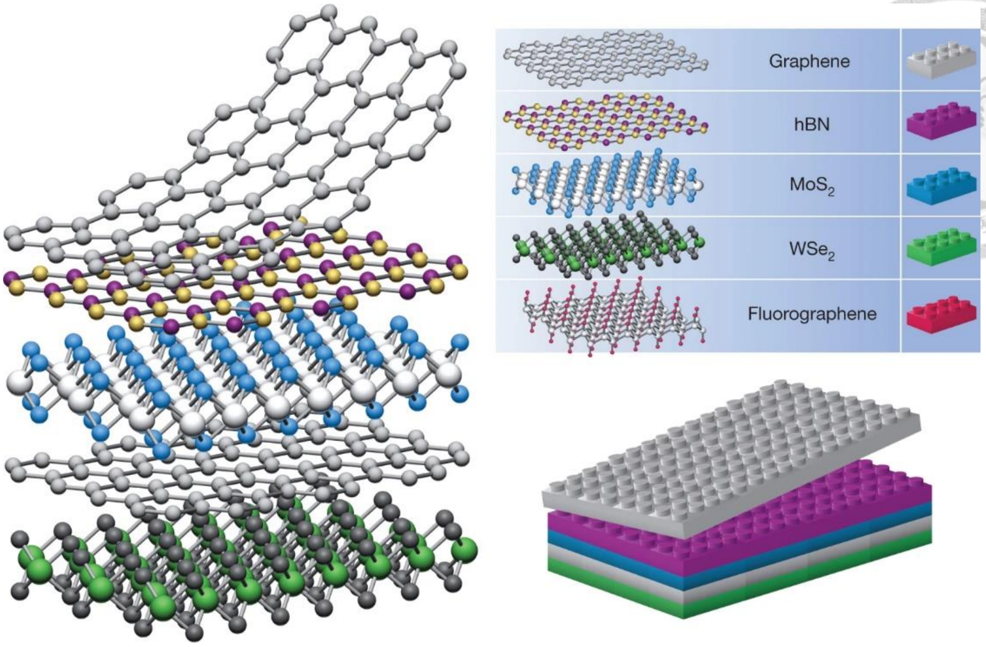

Figure 1.1-7 Building van der Waals heterostructures.[11]

1.2 Hydrogen evolution reaction (HER)

As energy consumption increases and environmental pollution worsens, it is essential to develop new energy sources to replace fossil fuels. Hydrogen is considered a sustainable energy carrier for future energy systems. The splitting of water is the best method for producing hydrogen fuel from electrical energy. In this process, water is the primary source, generating hydrogen (H_2) and oxygen (O_2) as the by-products. Generally, water splitting is divided into two half-reactions: Oxygen Evolution Reaction (OER) at the anode and Hydrogen Evolution Reaction (HER) at the cathode. As illustrated in **Figure 1.2-1**, water molecules decompose into hydrogen and oxygen when a voltage is applied to the electrode. The produced hydrogen can be stored as fuel, while oxygen can be released into the atmosphere[46].

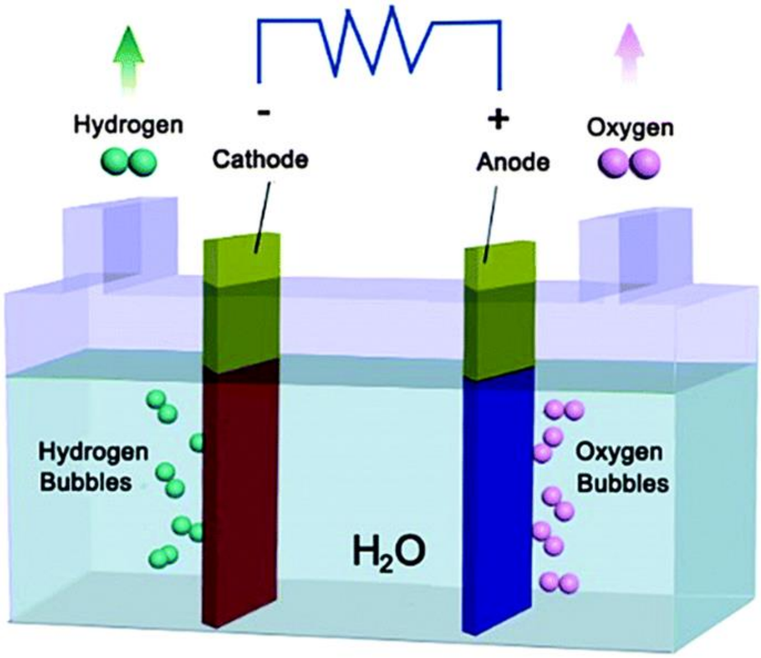

Figure 1.2-1 Schematic diagram of water splitting.[46]

This thesis focuses on HER and its catalyst, which is the simplest electrocatalytic reaction. Excellent HER electrocatalysts require performance conditions such as high electronic conductivity, good surface structure, abundant electrocatalytic active sites, electrochemical stability, low overpotential, and low cost [47]. With the development of renewable energy sources, electrolytic production of hydrogen is becoming a viable alternative for producing hydrogen to power internal combustion engines and fuel cells [48].

doi:10.6342/NTU202402275

■Mechanism

Theoretical and experimental studies have examined the hydrogen evolution reaction (HER) mechanism in both acidic and alkaline environments. These investigations have explored the Volmer–Heyrovsky and Volmer–Tafel reaction in both acidic and alkaline conditions **(Figure 1.2-2)**[49]. The first step for HER in acidic condition is that the proton (H^+) adsorbs onto the catalyst surface and receives electrons released from the electrode to become adsorbed hydrogen (H*). The part of the surface that adsorbs hydrogen is called an active site, and this process is known as the Volmer reaction. The second step is the desorption of hydrogen gas (H_2), further divided into two types. One type is that two adsorbed hydrogen combine to generate hydrogen gas, called the Tafel reaction. The other type is a proton that receives electrons released from the electrode through the adsorbed hydrogen and combines with it to generate hydrogen gas. This is called the Heyrovsky reaction[50]. For acidic media,

$$H^+ + e^- \rightarrow H^* \text{ (Volmer)} \tag{1}$$

$$H^* + H^+ + e^- \rightarrow H_2 \text{ (Heyrovsky)} \tag{2}$$

$$2H^* \rightarrow H_2 \text{ (Tafel)} \tag{3}$$

In alkaline media, the hydrogen evolution reaction (HER) begins with the dissociation of H_2O molecules to provide protons. This process involves both Volmer reaction and

Heyrovsky reaction, while the Tafel step remains unchanged compared to the reaction in an acidic solution.[51] For alkaline media,

$$H_2O + e^- \rightarrow H^* + OH^- \text{ (Volmer)} \tag{4}$$

$$H^* + H_2O + e^- \rightarrow OH^- + H_2 \text{ (Heyrovsky)} \tag{5}$$

$$2H_2O + 2e^- \rightarrow 2OH^- + H_2 \text{ (Tafel)} \tag{6}$$

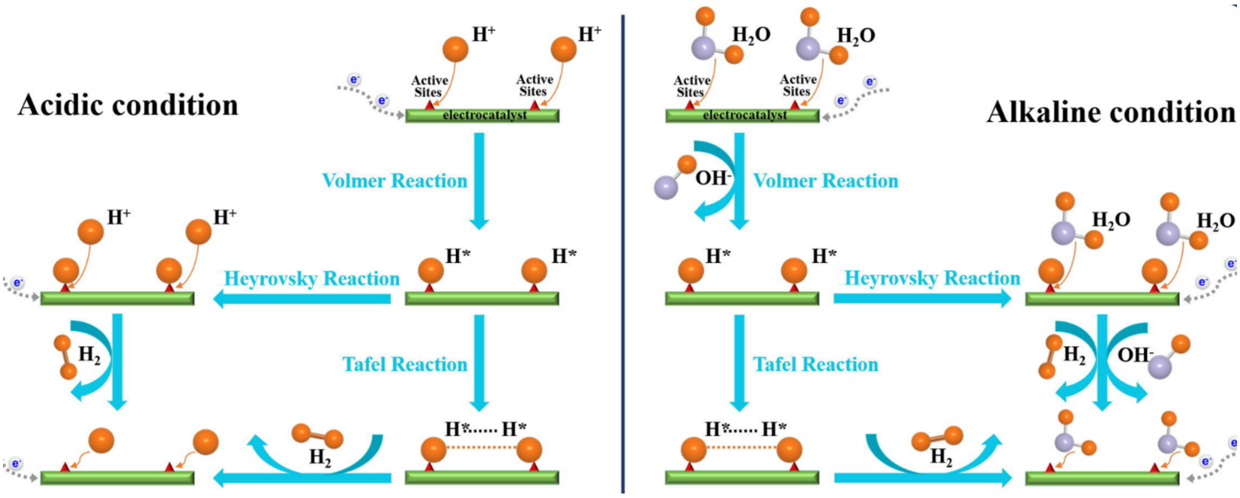

Figure 1.2-2 Mechanism of hydrogen evolution under acidic and alkaline conditions.[52]

[redacted]Overpotential and Tafel slope

HER was measured by Linear Sweep Voltammetry (LSV) to collect polarization curves of electrocatalysts. After normalizing the current in LSV, the polarization curve is represented by plotting the relationship between current density (j) and potential (V). A polarization curve showing lower potential at the same current density or higher current density at the same potential indicates that the studied electrocatalyst has better catalytic activity[53]. Overpotential and Tafel slope are two important values that indicate the efficiency of HER.

Overpotential (η) is the additional voltage beyond the thermodynamic requirement needed to drive an electrochemical reaction at a certain rate. It represents the extra energy input required to overcome kinetic barriers and make a reaction occur at a desired rate. To compare the activities between samples, two specific overpotentials in HER are often considered. One is the "onset overpotential," which is a poorly defined term. The other is the overpotential required for the electrocatalyst to achieve a current density of 10 mA cm^{-2}. Materials that can produce a low overpotential at higher current densities are considered ideal electrocatalysts.[54]

The Tafel plot illustrates the relationship between steady-state current densities and various overpotentials. Typically, the overpotential has a logarithmic correlation with the current density, and the linear portion of the Tafel plot is fitted to the Tafel equation:

$$\eta = a + b \log j$$

, where a = log of exchange current (j_0), j = current density and b = Tafel slope. From this Tafel equation, two crucial parameters can be derived: the Tafel slope (b) and the exchange current density (j_0). The Tafel slope is generally associated with the catalytic mechanism of the electrode reaction, while the exchange current density, obtained when

doi:10.6342/NTU202402275

overpotential is assumed to be zero, describes the inherent catalytic activity of the electrode material under equilibrium conditions. An ideal catalytic material would possess a high j_0 and a low Tafel slope[46].

■Gibbs free energy (ΔG_H^*)

The Sabatier principle[55, 56] explains that for efficient hydrogen evolution on an electrocatalyst surface, there needs to be an optimal binding strength between the adsorbed hydrogen and the catalyst. If the bonding is too strong, it hinders the desorption steps (Heyrovsky/Tafel reactions) required to release the hydrogen as gas. Conversely, if the bonding is too weak, it impedes the initial Volmer step where hydrogen adsorbs onto the catalyst surface.

The adsorption and desorption of hydrogen on the electrocatalyst can be quantified by the Gibbs free energy (ΔG_H^*). The kinetics of the overall hydrogen evolution reaction (HER) are governed by this ΔG_H^* value for hydrogen adsorption. For an effective catalyst, the binding energy to hydrogen should be finely balanced, avoiding extremes of both excessive strength ($\Delta G_H^* < 0$) and weakness ($\Delta G_H^* > 0$)[57], which can be shown in the volcano plot (**Figure 1.2-3)**. The volcano plots that catalyst activity arises because the Sabatier principle dictates that there is a sweet spot - neither too strong nor too weak binding of the key reaction intermediate (hydrogen in the HER case). Catalysts that hit this optimum moderate binding energy perform best such as Pt, resulting in the peak of the volcano curve. [58]

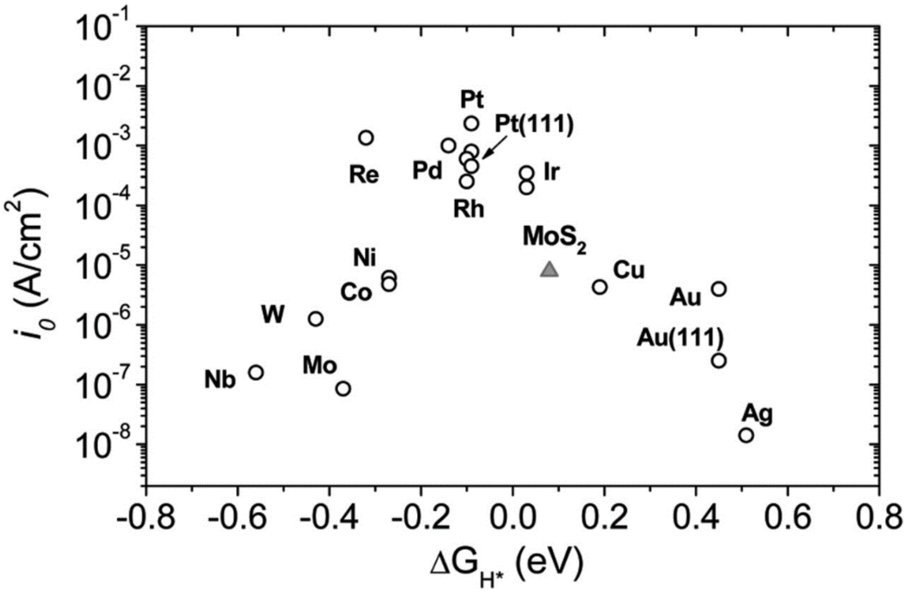

Figure 1.2-3 Volcano plot of the exchange current density as a function of the DFT-calculated ΔG_{H}^{*} of adsorbed atomic hydrogen for different materials.[59]

Turnover frequency (TOF)

In HER, turnover frequency (TOF) refers to the rate at which hydrogen molecules are produced per active site on the catalyst surface. It is a measure of the catalytic activity and efficiency of the catalyst for the HER. TOF is typically expressed as the number of hydrogen molecules produced per active site per unit time (e.g., molecules of H_2 s^{-1}). TOF was calculated from current densities (j) and the number of active sites, utilizing the following equation[59]:

$$\mathrm{TOF}(s^{-1}) = \text{Rate of hydrogen production (mol } H_2\ s^{-1}) \,/\, \text{Number of active sites}$$

$$= (\, j,\ \mathrm{A\ cm^{-2}})/\ [(\#,\ \mathrm{sites\ cm^{-2}})\ (1.602\times10^{-19},\ \mathrm{C/e^{-}})\ (2,\ \mathrm{e^{-}/H_2})]$$

A higher turnover frequency indicates that the catalyst is more efficient at producing hydrogen from the active sites. This metric is useful for quantitatively evaluating and comparing the performance of different catalysts for the HER and optimizing catalyst design and reaction conditions.

[redacted]HER of 2D materials and its edge

To reduce the reliance on Pt-based catalysts for hydrogen evolution reaction (HER), it is important to explore novel noble metal-free catalysts that are both cost-effective and highly efficient[60, 61]. 2D materials are considered promising candidates for electrochemical reactions, especially Molybdenum disulfide (MoS_2), due to the unique van der Waals layered structure, large exposed area[62], and superior catalytic activity[63-65]. As shown in **Figure 1.2-3**, the Gibbs free energy of MoS_2 is close to zero, similar to Pt-based catalysts, making it suitable for HER. However, the unsatisfactory electrical conductivity and a deficiency in active sites of pristine MoS_2 restrict the kinetics of the reaction process[66, 67]. Despite significant research, however, the activity of 2D material edges remains below noble metal catalysts. (**Figure 1.2-4a and 4b**). Substantial efforts have been dedicated to enhancing the catalytic performance of MoS_2 through two primary avenues (**Figure 1.2-4c**). One strategy involves increasing the number of active sites by introducing defects[68] and sulfur vacancies[69], or maximizing exposed edges which is linearly correlated with the activity of MoS_2[59, 70, 71]. The other strategy focuses on improving the intrinsic activity of the catalyst through the creation of heterostructures[72, 73] or the implementation of doping[74]. A promising route to enhance the catalytic performance of 2D materials could be oriented external electric fields (OEFs), which will be further discussed in the following section.

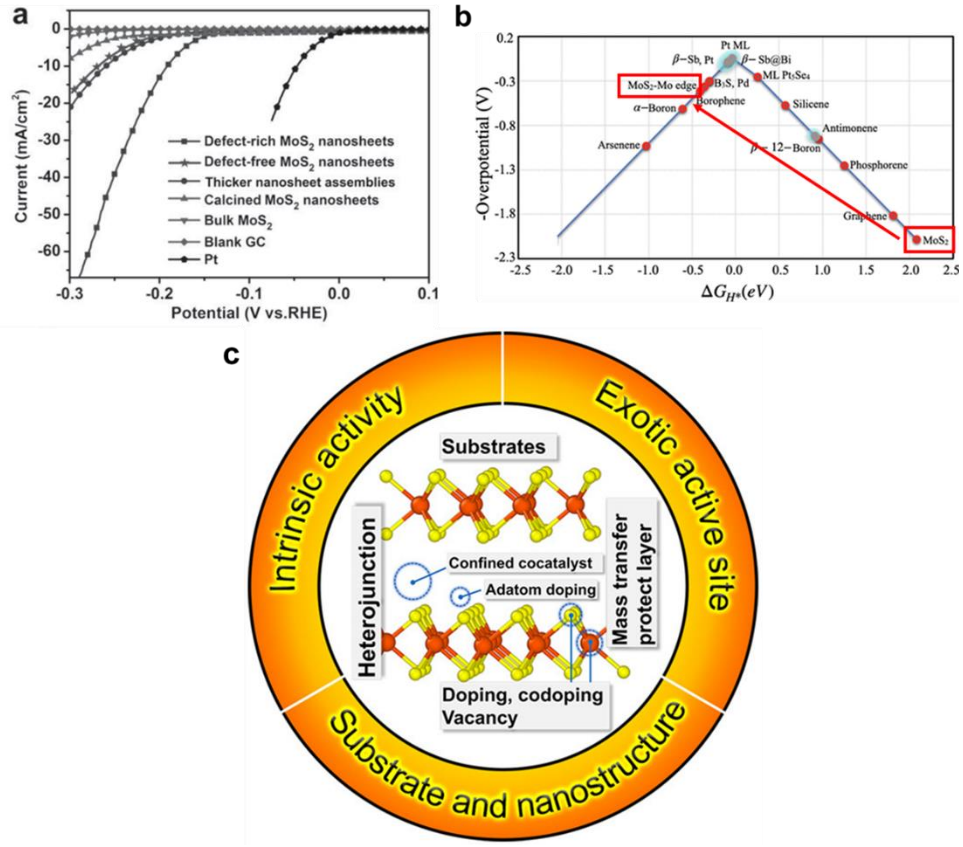

Figure 1.2-4 (a) Polarization curves of different nanosheets.[65] (b) HER volcano curve of previously reported list of 2D layered materials including the most commonly used Pt.[75] (c) Strategies for enhancing the HER of 2D materials.[76]

doi:10.6342/NTU202402275

1.3 Oriented electric field (OEF)

An Oriented Electric Field (OEF) represents the local electric field experienced by individual units or dipoles within the material, considering the effects of the material's polarization and internal electric fields. This precise orientation allows researchers to investigate and manipulate various properties effectively. It can redistribute electronic charges within molecules, reorient molecular dipoles, and influence chemical reactions by directing pathways and lowering activation energies [77, 78]. Oriented Electric Fields have been reported to enhance oxygen evolution reaction[79], organic reactions,[80] carbon nanotube growth,[81] and carbon dioxide activation.[82]

OEFs seem to be particularly well suited for hydrogen evolution reactions (HER) due to the importance of properly oriented bonds in the proton transfer process**(Figure1.3-1a)**[83]. OEF-induced variations of the homogeneous charge distribution within the double layer **(Figure1.3-1b)**[84] could lower the energetic cost of reorienting individual protons within the collective dipole of the double layer and decrease the energetic barrier of reactant motion **(Figure1.3-1c and 1d)**.[83]

doi:10.6342/NTU202402275

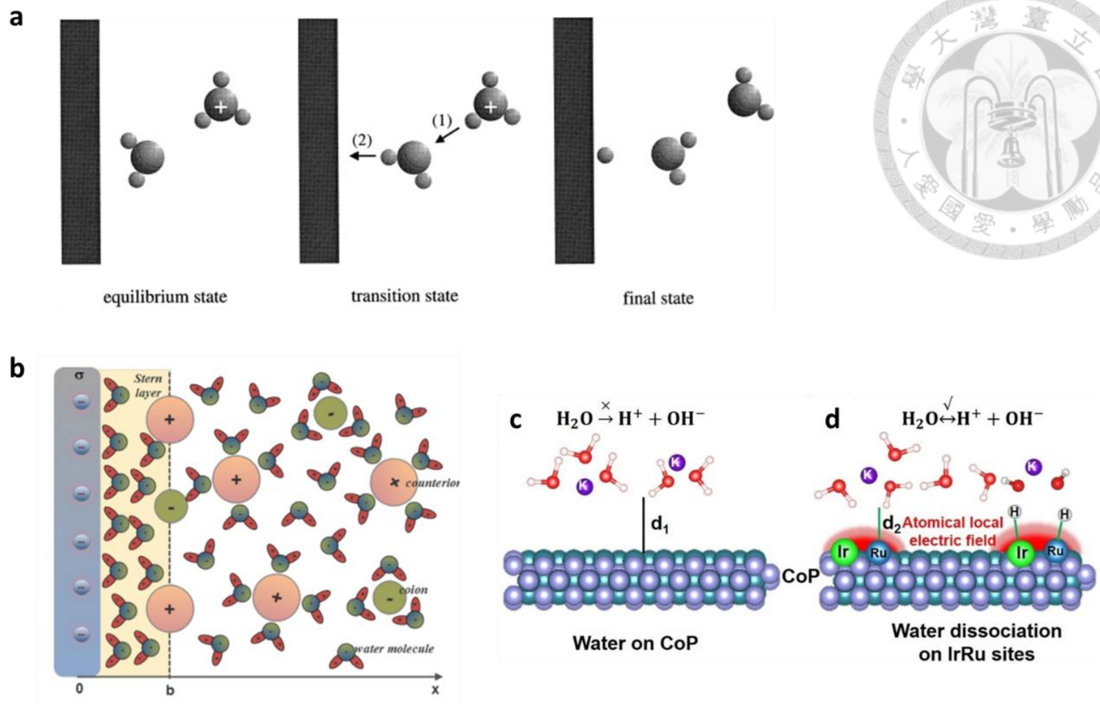

Figure 1.3-1 (a) Typical configurations of the proton transfer in Volmer reaction.[84] (b) Electric double layer (EDL) (c) Schematic of interface H_2O reorientation induced by OEF on CoP and (d) IrRu DSACs.[83]

1.4 Motivation

Electrochemical reactions are at the heart of efforts to convert sustainable energies into needed products, such as fuels and chemicals.[85] Achieving the necessary scale to make a global impact requires noble metal-free catalysts with high efficiency and low cost.[86, 87] 2D materials edges have demonstrated great potential in electrocatalysis due to their high surface area, large tunability of chemical character, and superior catalytic activity.[62, 88] Despite significant research, however, the activity of 2D material edges remains below noble metal catalysts.[89]

A promising route to enhance the catalytic performance of 2D materials could be oriented electric fields (OEFs).[77, 78] Through electrostatic modification of the bond alignment between catalyst and reactant, the efficiency and selectivity of chemical reactions can be enhanced.[90]

Recent findings on 2D materials subjected to external field modulation[91, 92] and defect-assisted internal field engineering [93, 94] indicate the potential impact of OEFs on the electrochemical reactivity of 2D materials. Unfortunately, the described approaches are only able to enhance the reactivity of a 2D material's basal plane and not its edge. Therefore, the observed enhancements have been limited by the low initial electrocatalytic activity of the basal plane compared to 2D materials edges.[95] In this thesis, we here demonstrate the realization of OEFs at the 2D material edge and its impact on electrochemical performance through the design of a vertical heterojunction.

doi:10.6342/NTU202402275

Chapter 2　Experimental Process and Apparatus

2.1 Experimental Process

■Synthesis of Graphene

The copper foil (Alfa Aesar 46365, purity 99.8%) served as the CVD-graphene growth substrate. Adhering to a previously reported methodology, the copper foils piled up between graphite foil in 1 inch quartz tube **(Figure 2.1-1a)** were first annealed at 1020 °C for 70 minutes under 10 sccm H_2. The growth of graphene was initiated by introducing a gas mixture comprising 200 sccm H_2 and 10 sccm CH_4 at 1020 °C for 6 hours. Subsequently, the sample was gradually cooled to room temperature at a rate of 10 °C/min under 10 sccm H_2. **(Figure 2.1-1b)**

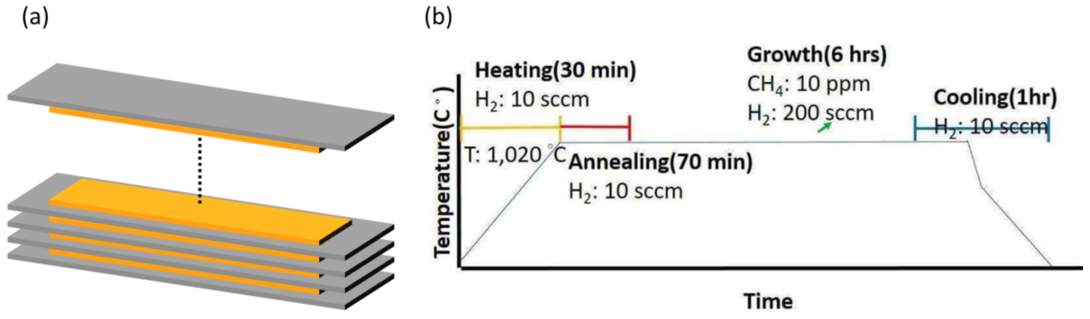

Figure 2.1-1 (a) The schematic diagram of stacking of graphite and copper foil **(b)** Graphene growth condition

■Synthesis of MoS_2

We use a chemical vapor deposition (CVD) system to synthesize uniform MoS_2 film. Initially, Si substrate with a 300 nm SiO_2 film was treated as the growth substrate, which implemented pre-cleaning procedures, involving a 5-minute sonication in acetone, followed by a 10-minute oxygen plasma treatment. Subsequently, a spin-coated solution of sodium chloride (0.01 g ml^{-1} NaCl and 2.5×10^{-4} M NaOH) was applied to the substrate to facilitate growth. Graphite foil with 40 nm molybdenum trioxide (MoO_3) deposited by e-beam evaporation, serving as the molybdenum (Mo) precursor, was oriented face down towards the substrates. This assembly was placed inside the 3 inch quartz tube in the center of the furnace.

MoS_2 growth followed a two-step heating process. All the processes were under 350 sccm H_2S (1% H_2S + 99% Ar). First, the temperature was ramped up to 700 ℃ in 20 minutes. Second, the temperature was further increased from 700 ℃ to 900 ℃ in an additional 20 minutes. Then, the growth temperature was held at 900 ℃ for 10 minutes. Following this two-step heating process, the samples underwent a gradual cooling process to reach room temperature.

doi:10.6342/NTU202402275

Transfer Process

For additional experimental requirements following graphene synthesis, the material must be transferred onto a Si/SiO_2 substrate. Initially, a layer of polymethyl methacrylate (PMMA) is applied onto the sample via spin-coating and subsequently dried for one hour at 65°C. This PMMA layer serves as a supportive medium during the etching process. Next, the copper foil is immersed in an ammonium persulfate (APS) solution until completely dissolved, leaving the graphene to be lifted onto the designated substrate, where it is dried for an additional hour at 65°C. Lastly, the sample undergoes immersion in acetone to remove the PMMA layer **(refer to Figure 2.1-3).**

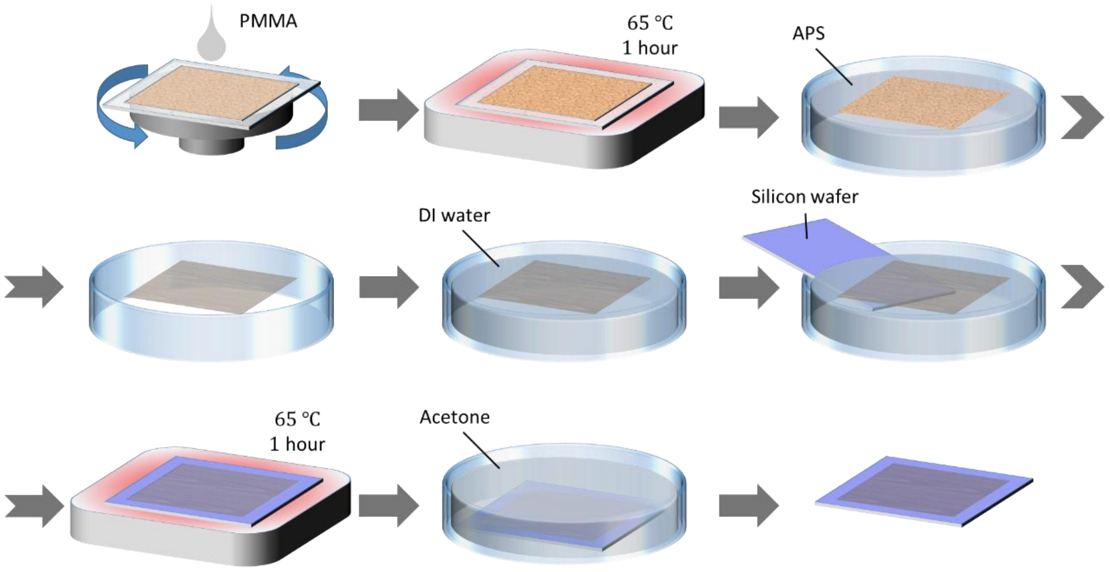

Figure 2.1-2 The schematic diagram of the transfer process of graphene

To fabricate the MoS_2/graphene heterostructure, a similar transfer process is conducted for the MoS_2 material. Initially, PMMA is spin-coated onto the MoS_2 sample on a Si/SiO_2 substrate and dried for an hour at 65°C, acting as a protective layer. Subsequently, the sample is soaked in a 1M NaOH solution for several hours. Following this, the MoS_2 adhered to the PMMA layer floats atop the solution due to the Si etching caused by the base, allowing it to be retrieved using a PET film and transferred onto the graphene layer and baked for an hour at 65°C. Finally, the sample undergoes acetone immersion to remove the PMMA layer.

[redacted]Patterning of nanoribbon

To create MoS_2/graphene/fluorographene heterojunction nanoribbon patterns, graphene was transferred onto Si/SiO_2/MoS_2 substrates using a well-established wet chemical process (**further details in section 2.1.3**). Following this, a 25 W CF_4 corona discharge plasma was utilized to pattern both the multilayer graphene and graphene wrinkles, operating under a pressure of 600 mTorr for 10 minutes until the distinctive Raman signal of the monolayer graphene region disappeared **(Figure 2.1-3)**.

For the patterning of MoS_2 nanoribbons, the graphene/fluorographene portion of the heterojunction was removed through a 40-second treatment with oxygen plasma.

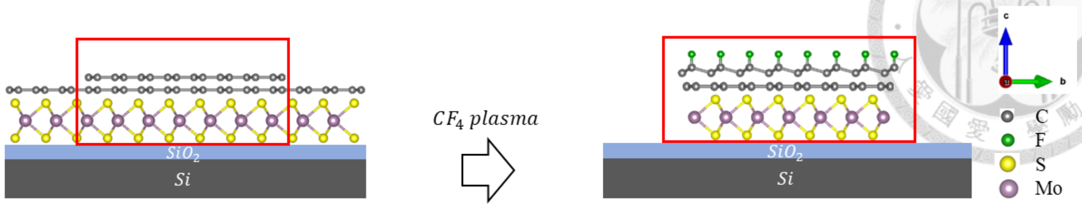

Figure 2.1-3 The schematic illustration of fabricating MoS_2/graphene/fluorographene nanoribbon by CF_4 plasma, showing that MoS_2 covered by bilayer graphene remains after CF_4 plasma treatment.

[redacted]Electrochemical measurement

2.1.5.1 Experimental Setup

The sample underwent measurement using a three-electrode system on the CH electrochemical station. The counter and reference electrodes were made of platinum (Pt) and silver/silver chloride (Ag/AgCl), respectively. A pre-fabricated gold electrode on the sample served as the working electrode, which was coated with photoresist to ensure that all contributions to the hydrogen evolution reaction originated from the catalyst in the exposed window. (**Figure 2.1-4**)

doi:10.6342/NTU202402275

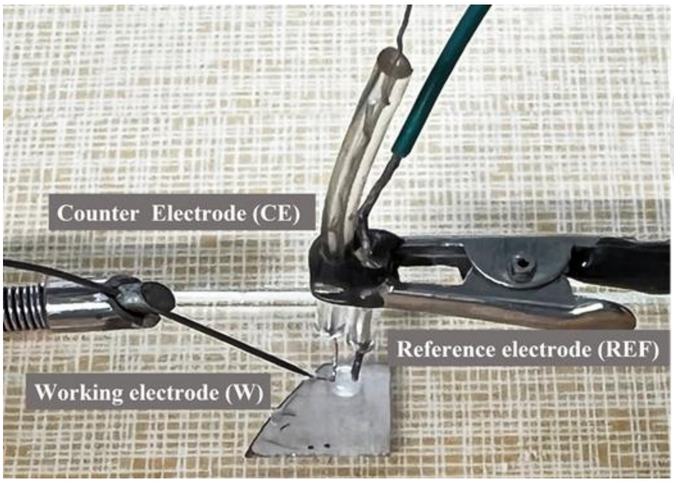

Figure 2.1-4 Setup for three-electrode system

2.1.5.2 Linear Sweep Voltammetry (LSV)

We uses Linear Sweep Voltammetry (LSV) to collect the polarization curves of electrocatalysts, which are represented by plotting the relationship between current density and potential. Polarization curves were recorded in a 0.5 M H_2SO_4 solution at a scan rate of 0.07 V s^{-1}, with the applied voltage ranging from 0 V to -2 V. All potentials reported in our study were referenced to the reversible hydrogen electrode (RHE), calculated using the equation: E(RHE) = E(Ag/AgCl) + 0.197 + Vquasi + 0.05pH.

2.1.5.3 Electrochemical impedance spectroscopy (EIS)

Electrochemical impedance spectroscopy (EIS) analysis is employed to understand the kinetics of HER and the reactions occurring at the interface between electrode and

doi:10.6342/NTU202402275

electrolyte. EIS was conducted across a frequency range from 1 Hz to 1 MHz, using an amplitude of 0.5 V. Measurements were performed at an overpotential of -0.8 V in a 0.5 M H_2SO_4 solution.

2.1.5.4 Details of data processing

The current density within the nanoribbon array was calculated according to

$$J = \frac{n_{NR} A_{NR}}{A_{window}} I$$

, where n_{NR} is the number density of nanoribbons, A_{NR} is the average area of one nanoribbon, and A_{window} is the area of the exposed microelectrode. The parameters for n_{NR} and A_{NR} are extracted from statistical analysis of atomic force micrographs and transmission electron micrographs and we utilize a nanoribbon width of 100nm and a length of 10um.

The extracted current density does not consider selective reactions at the edges and thus only provides a lower boundary for the reaction current. Despite this limitation, the extracted current density is significantly enhanced, demonstrating the impact of the increased edge reactivity. Previous work has suggested a hundredfold increased activity of edges compared to the basal plane[96], indicating that the current density for exclusive edge-based HER would be 30x higher.

To calculate the turnover frequency, we again utilize a conservative estimation procedure. We normalize the reaction current by both MoS_2 edge atoms and F-atoms. To calculate the number of edge-bound Mo atoms, we divide the perimeter of a nanoribbon by the MoS_2 lattice constant, while the F-atom density was derived to be 25% of the basal plane carbon atom concentration based on XPS characterization[34]. This approach assumes identical turnover frequencies for F-atoms and MoS_2 edges, which provides a lower estimate of the TOF. Previous reports demonstrated the limited HER activity of fluorographene[97], which suggests that the real TOF of MoS_2 edges could be up to 150x higher.

Turnover frequencies were calculated from current densities (j) and the number of active sites, utilizing the following equation[59]:

$$\mathrm{TOF}(\mathrm{s}^{-1}) = (\, j,\ \mathrm{A\ cm}^{-2}) / [(\#,\ \mathrm{sites\ cm}^{-2})\ (1.602\times10^{-19},\ \mathrm{C/e}^{-})\ (2,\ \mathrm{e}^{-}/\mathrm{H}_2)]$$

Finite-element simulation of electrostatics

Electrostatic simulations were conducted using Comsol Multiphysics 5.2. The Poisson equation was numerically solved assuming a potential difference between two 1nm thick layers with micrometer width. Graphene was employed as the middle layer of the capacitor and the whole structure was surrounded by water. The dielectric constants were extracted from literature.

[redacted]DFT calculation methods

All calculations were performed using the atomistic simulation software QuantumATK (version T-2022.03), employing a numerical LCAO basis set. The generalized gradient approximation (GGA) with the Perdew-Burke-Ernzerhof (PBE) functional was utilized to handle exchange-correlation interactions in all calculations. Convergence thresholds for fluorographene, graphene, and MoS_2 were set to 0.05 eV $Å^{-1}$ for atomic forces, with a tolerance accuracy of 0.0027 eV for the self-consistent-field (SCF) loop. To simulate heterojunction nanoribbons, the 3D periodic boundary contained at least 15 Å of vacuum space to prevent interactions between layers and nanoribbons. The dimensions of both unit cells are fixed at 0.948 nm (A axis), 2.94 nm (B axis), and 4.00 nm (C axis).

Our calculations involved the construction and optimization of fluorographene, graphene, and MoS_2 individually, followed by the construction of a heterostructure. For the heterojunction nanoribbon model **(Figure 2.1-5)**, the top layer comprised one-side-saturated fluorinated graphene, while the second layer consisted of pure graphene, which underwent optimization. To minimize the lattice mismatch between graphene and MoS_2[98], we enlarged the lattices of graphene and MoS_2 by four times and three times, respectively, to build the heterojunction nanoribbon structure. To gain further insights into the interaction and energy between hydrogen and the nanoribbon, a hydrogen atom was placed adjacent to the basal plane and edges of each layer individually, and the total energy for each model was calculated. Finally, following the methodology outlined in Nørskov et al.[58], the Gibbs free energy of the hydrogen atom was determined.

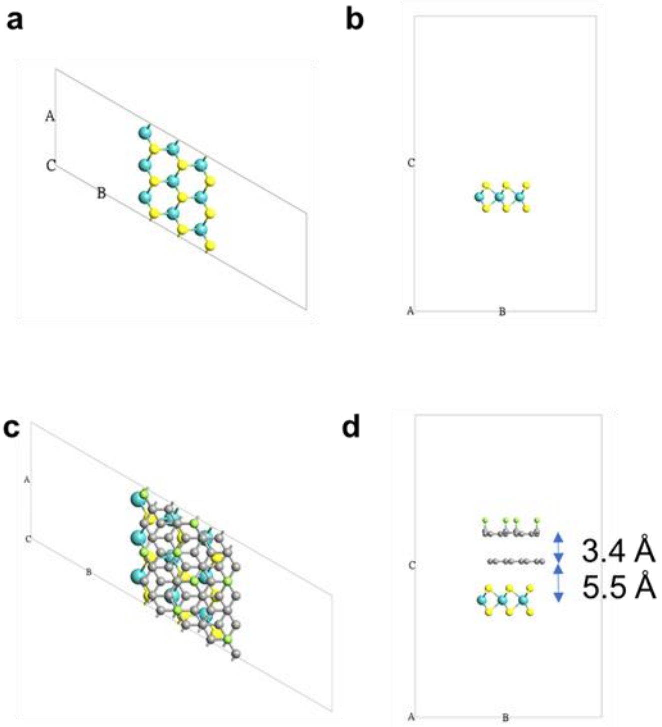

Figure 2.1-5 Model of (a, b) MoS2 nanoribbon and (c, d) heterostructure nanoribbon. Elements: blue, Mo; yellow, S; green, F.

2.2 Apparatus

■Chemical Vapor Deposition (CVD) system

Figure 2.2-1 shows the chemical vapor deposition high-temperature furnace (APCVD) used in this experiment. Chemical Vapor Deposition (CVD) is a process used to produce high-quality, high-performance solid materials. In our experiment, the growth environment is conducted at atmospheric pressure (APCVD). The CVD furnace has three heating zones, and quartz tubes with a diameter of one inch are used for both growth and annealing processes. The gas inlet is on the right side, with the sample placed in the middle heating zone, and the gas outlet is on the left side. CVD involves the reaction of gaseous precursor compounds to form a solid material on a substrate surface. The process is typically carried out in a heated chamber where the precursors are introduced, allowing for controlled deposition and growth of thin films or coatings.

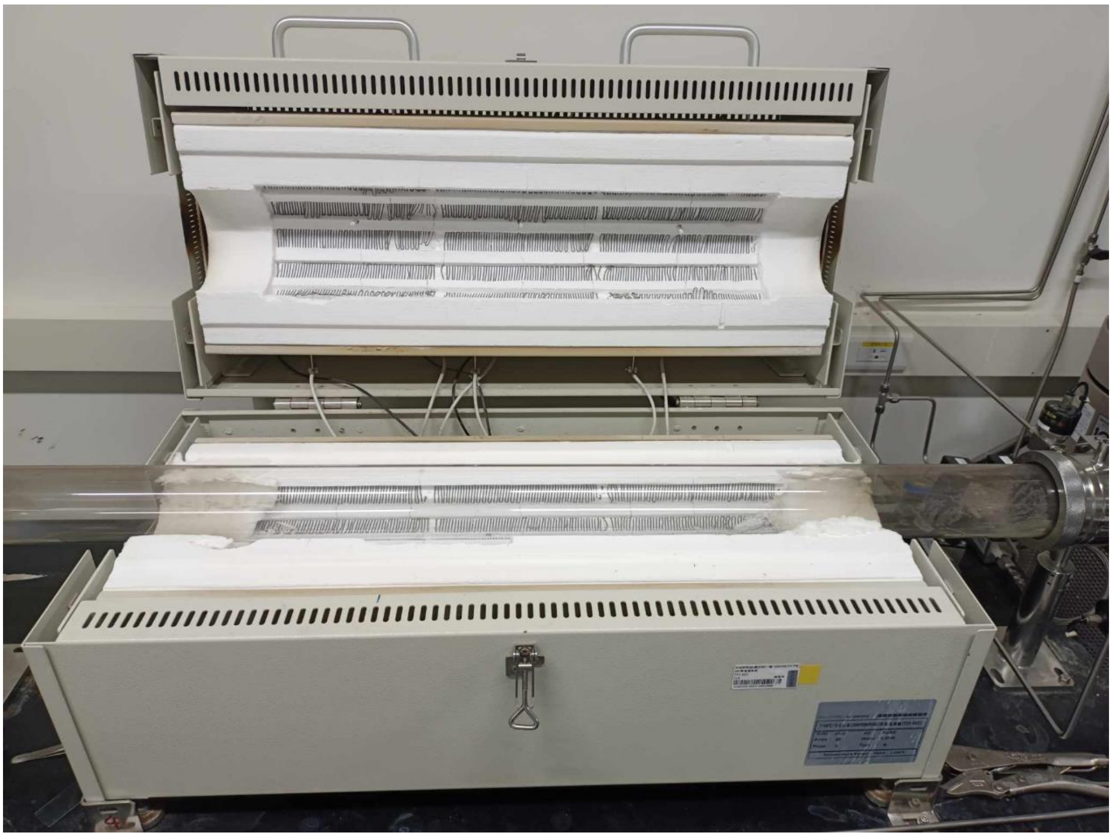

Figure 2.2-1 CVD furnace for graphene and MoS_2 synthesis

doi:10.6342/NTU202402275

■Thermal Evaporator

The thermal evaporation system depicted in Figure 2.2-2 is used to deposit gold electrodes. This system works by applying a high current to heat a tungsten boat containing the target material. When the required temperature is reached, the material evaporates and condenses onto the substrate surface. A film thickness gauge incorporating a crystal oscillator monitors the thickness of the deposited material layer. As material accumulates on the oscillator crystal, its vibration frequency shifts, allowing the film thickness to be calculated based on this frequency change.

Figure 2.2-2 Thermal evaporator system

■Photolithography

The photolithography setup shown in Figure 2.2-3 utilizes a Dell M115HD projector as

doi:10.6342/NTU202402275

the light source, allowing custom mask designs to be projected onto the sample. The process begins by coating the sample with a photoresist material, which is then heated for one minute. Next, light from the projector is exposed through the designed mask pattern onto the photoresist-coated sample. This light exposure alters the solubility of the photoresist in the developer solution. There are two types of photoresists - positive and negative. For this study, a positive photoresist is employed, where the exposed regions become soluble and can be selectively removed after development.

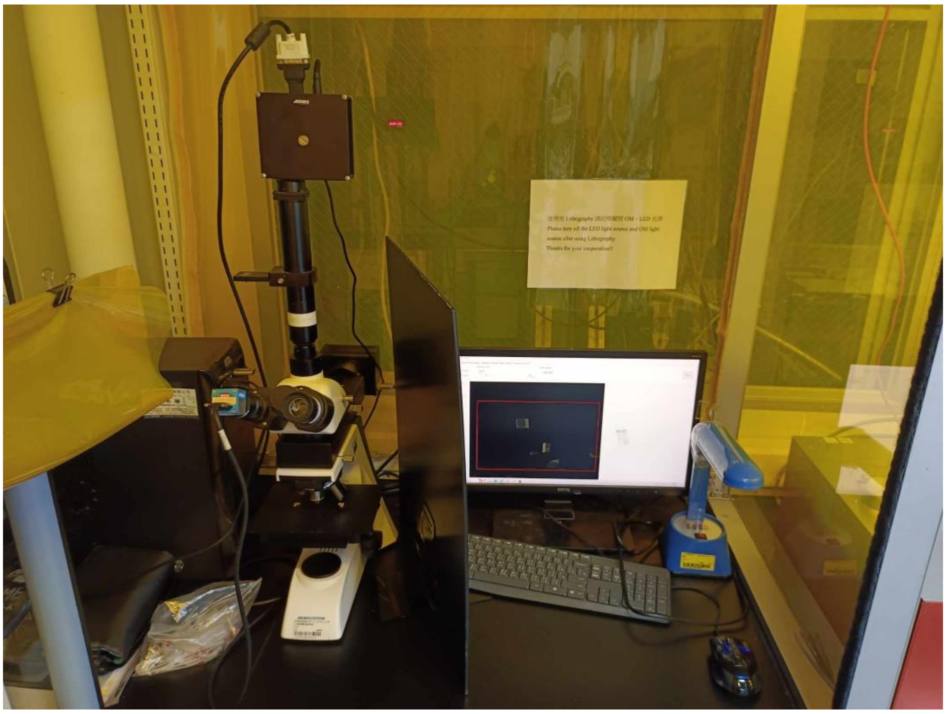

Figure 2.2-3 Photolithography system

Plasma system

Figure 2.2-4 depicts the CF_4 and O_2 plasma system used for physical etching, which is a PDC 32-G model from Harrick Plasma. In this system, atoms become ionized through repeated collisions driven by an applied electric field. When these energetic argon ions strike the material surface, they physically dislodge and remove some of the surface atoms through momentum transfer. As this process continues over time, the surface gradually becomes cleaned and etched away.

Figure 2.2-4 Argon plasma system

[redacted]Raman system and optical microscope

Figure 2.2-5 shows the Raman setup in our lab, which includes an Olympus BX53 optical microscope, a PIXIS 100B CCD, an Acton Series SP-2150i spectrometer, and a 532nm green light laser (SLD-532-SLM-100T) from Dream Laser.

In the Raman system, when a beam of light is directed at a material, the photons interact with the material, causing a change in the frequency of the reflected light. The difference in wavenumber between the excitation light and the reflected light is known as the Raman shift.

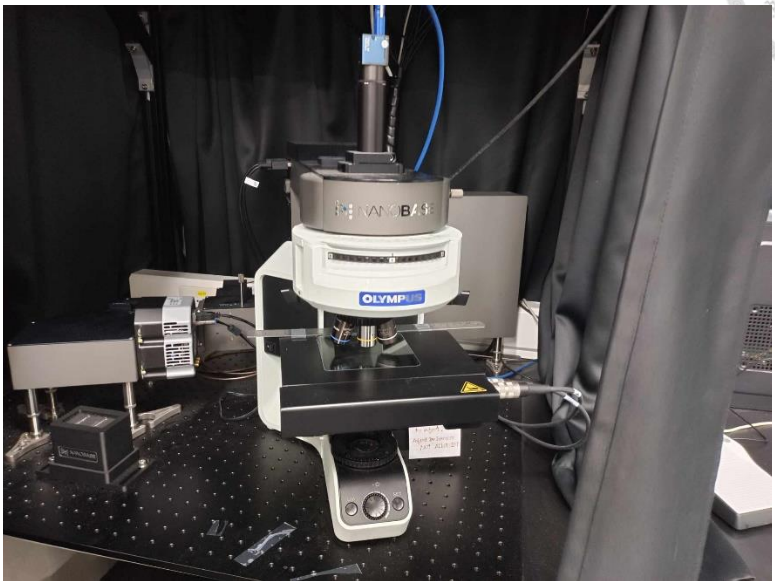

Figure 2.2-5 Raman system

Atomic Force Microscope (AFM)

Figure 2.2-6 shows the AFM system (FORCE AFM GENIE E7) used to measure the thickness of the material. This system employs a vibrating tip during scanning, and the detector collects the signal from the laser reflected off the tip. As the sample thickness varies, the reflecting angle of the laser changes, allowing us to determine the thickness of the material.

Figure 2.2-6 AFM system

Transmission Electron Microscope (TEM)

To perform detailed investigations into the crystal structure of samples, transmission electron microscopy (TEM) is employed. In this technique, an electron beam is transmitted through the sample mounted on a mesh grid, producing a diffraction pattern that can be analyzed and used for characterization purposes.

Two main functions of the TEM are commonly utilized - diffraction contrast imaging and selected area electron diffraction (SAED). Diffraction contrast imaging allows researchers to study the spacing between atomic planes or layers within the crystal. Fast Fourier transforms (FFTs) can also be applied to these images for further structural analysis. On the other hand, SAED yields a diffraction pattern in reciprocal space that

doi:10.6342/NTU202402275

is characteristic of the material's crystal structure. From the spacing between the bright diffraction spots in the SAED pattern, researchers can extract information about the interplanar distances (d-spacings) within the crystal lattice.

In this study, the TEM image and SAED are carried out by High-Resolution Transmission Electron Microscopy (JEM2100F).

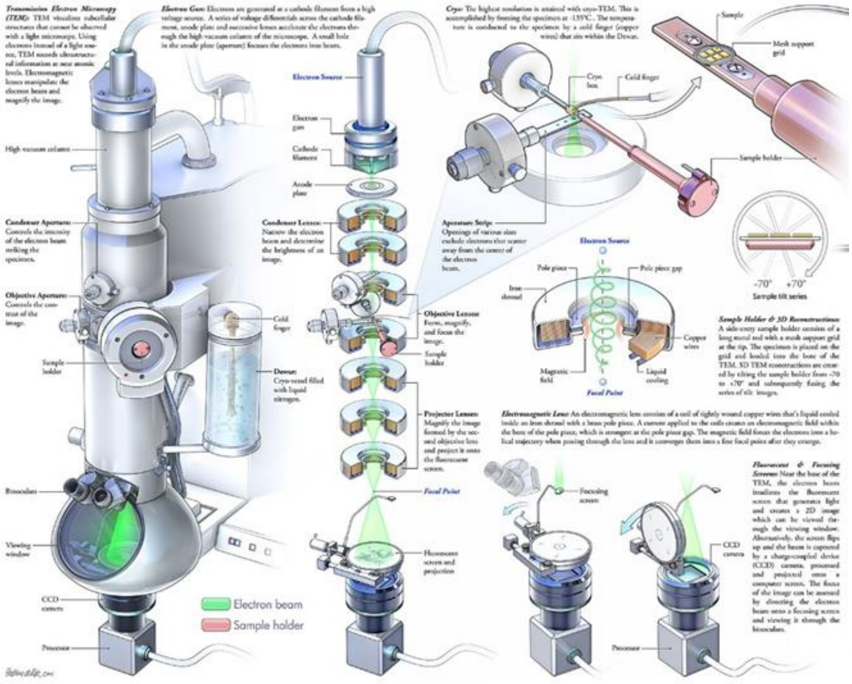

Figure 2.2-7 The structure of TEM [28]

Scanning electron microscopy (SEM)

Scanning Electron Microscope (SEM) data were collected by Bruker’s Dimension Icon and FESEM Nova 450. Scanning Electron Microscopy (SEM) is a powerful imaging technique that uses a focused beam of high-energy electrons to create detailed images of a sample's surface. SEM offers high resolution and depth of field, making it essential in materials science. It works by detecting signals such as secondary and backscattered electrons produced when the electron beam interacts with the sample. SEM can reveal surface structures at the nanometer scale but requires sample preparation, such as coating non-conductive samples with a conductive material and operating in a vacuum environment.

[redacted]Electrochemical workstation

The electrochemical instrument used in this laboratory is manufactured by CH Instruments, model CHI-660E. The system includes a fast digital signal generator, fast data acquisition circuits, a potentiostat, and a galvanostat. It supports various electrochemical analysis functions such as open circuit potential measurement, cyclic voltammetry (CV), linear sweep voltammetry (LSV), Tafel plot analysis, and various electrochemical impedance spectroscopy techniques. These capabilities enable comprehensive electrochemical, corrosion, and battery-related research.

doi:10.6342/NTU202402275

Figure 2.2-8 Electrochemical workstation

[redacted]Electrical measurement system

Figure 2.2-9 shows the system used for current-voltage (I-V) measurements, which is a Keysight B2912A source/measure unit. The probes employed in this setup are fabricated from tungsten. By integrating an optical microscope into the system, precise positioning and contact of the probes with the sample can be achieved through direct visual guidance. This allows accurate I-V characterization to be performed by sourcing and measuring the current and voltage across the sample or device under test using the Keysight instrument.

doi:10.6342/NTU202402275

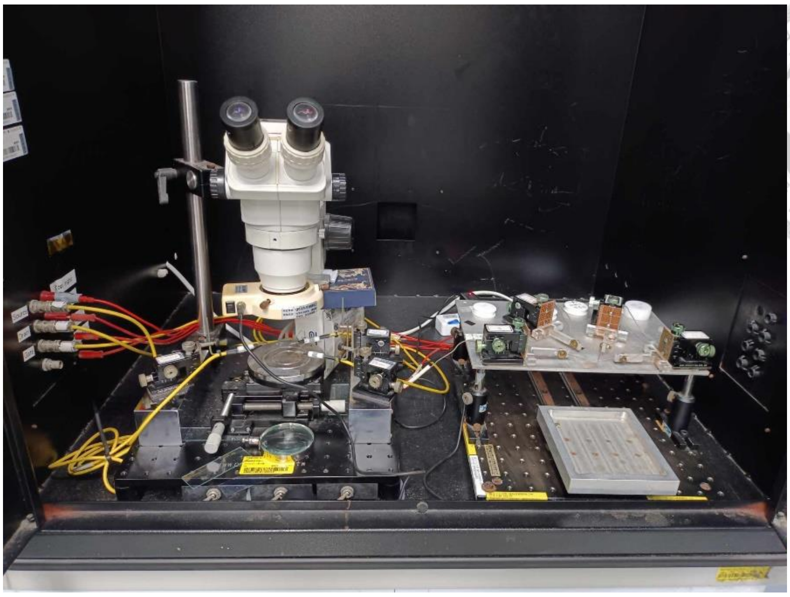

Figure 2.2-9 Electrical measurement system

doi:10.6342/NTU202402275

Chapter 3 Results and Discussion

We here demonstrate the realization of OEFs at the 2D material edge and its impact on electrochemical performance. Through the design of a vertical heterojunction, a permanent internal electric dipole can be produced. A bottom-up patterning process was utilized to convert the 2D heterojunction into nanometer-wide ribbon arrays whose electrostatics is dominated by fringing fields at their edges. Optical and impedance spectroscopic characterization at the vertical MoS_2/graphene/fluorographene edge confirms the formation of a sizable in-plane dipole that enhances the heterogeneous charge transfer reaction by two orders of magnitude. The presented OEF-enhanced 2D edge reactivity was applied to hydrogen evolution reactions (HER), where ab initio calculations suggest a field-induced lowering of the hydrogen adsorption energy. Experimental HER confirms the impact of OEFs on MoS_2 edge reactivity and produces a 30% decrease in Tafel slope compared to pristine edges and an unprecedented turnover frequency for 2D materials-based electrocatalysts. Our results open up a new route to enhancing the prospect of 2D materials for electrocatalytic and photocatalytic generation and storage of energy.

doi:10.6342/NTU202402275

3.1 Formation of 2D heterojunction nanoribbons [redacted] patterning process

We create heterojunctions by sequentially transferring CVD-grown MoS_2 and graphene onto a SiO_2/Si substrate (**Figure 3-1-1a**), then integrate vertical 2D heterojunctions and edge-dominated electrochemistry into heterojunction nanoribbons using a self-aligned bottom-up patterning technique (**Figure 3-1-1b**). This method transforms vertical 2D heterojunctions into nanoribbons that mimic the contours of graphene wrinkles. Graphene wrinkles, with nanometer-scale width and a high aspect ratio, naturally form due to the thermal expansion coefficient mismatch between the copper growth substrate and graphene during the cooling process following growth. Scanning electron micrographs confirm the formation of extensive arrays of parallel wrinkles after chemical vapor deposition (CVD) growth (**Figure 3-1-1c**). Upon transfer from their growth substrate, capillary forces cause these wrinkles to collapse, resulting in trilayer graphene (TLG) nanoribbons within the single-layer graphene (SLG).[34]

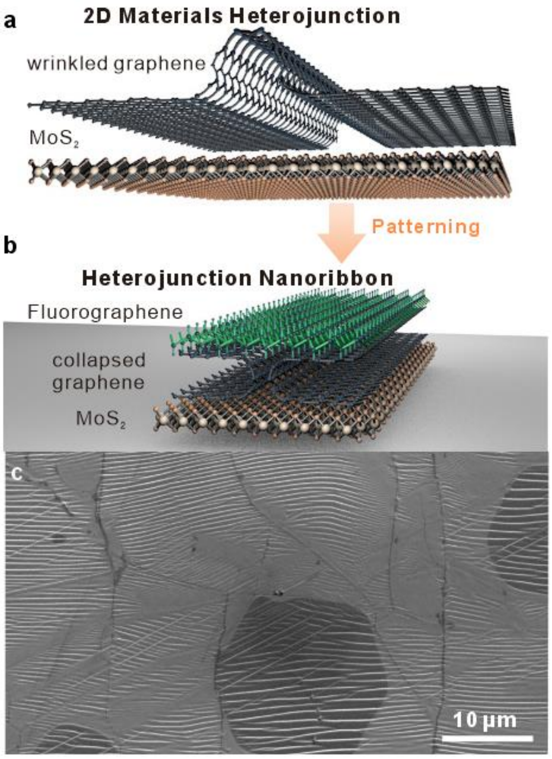

Figure 3.1-1 (a) Schematic illustration of thickness-dependent pattern transfer process. (b) Resulting MoS$_2$/graphene/fluorographene heterojunction nanoribbon. (c) Scanning electron micrograph of CVD-grown graphene on copper foil.

Characterization

3.1.2.1 OM and Raman

As the optical micrographs shown in **Figure 3.1-2**, our initial step involved transferring CVD-grown graphene onto the surface of MoS$_2$ (**Figure 3.1-2a**). After the CF$_4$ plasma treatment, the area covered by monolayer graphene is etched, while regions with bilayer or multilayer graphene remain unaffected (**Figure 3.1-2b**). This phenomenon arises due to the functionalization of the top layer of graphene with fluorine, creating a mutual stabilization effect between the two graphene layers, which leads to atomically abrupt transitions[1].

Raman spectroscopy **(Figure 3.1-2c**), measured before and after the etching process, showed the presence of characteristic in-plane (E_{2g}) and out-of-plane (A_{1g}) phonon vibration modes for pristine 2H phase MoS_2, located at 384 cm^{-1} and 407 cm^{-1}, respectively, as well as the graphene G-band around 1590 cm^{-1}.

Additionally, we utilize Raman spectroscopy to analyze the constituents of the heterojunction. Deconvolution of Raman spectra reveals the presence of MoS_2 features alongside the graphene G-Band, consistent with expectations. The prominent presence of a D-Band and a broad G-Band feature suggests the conversion of the upper graphene layer into fluorographene, aligning with prior observations (**Figure 3.1-2d**).

doi:10.6342/NTU202402275

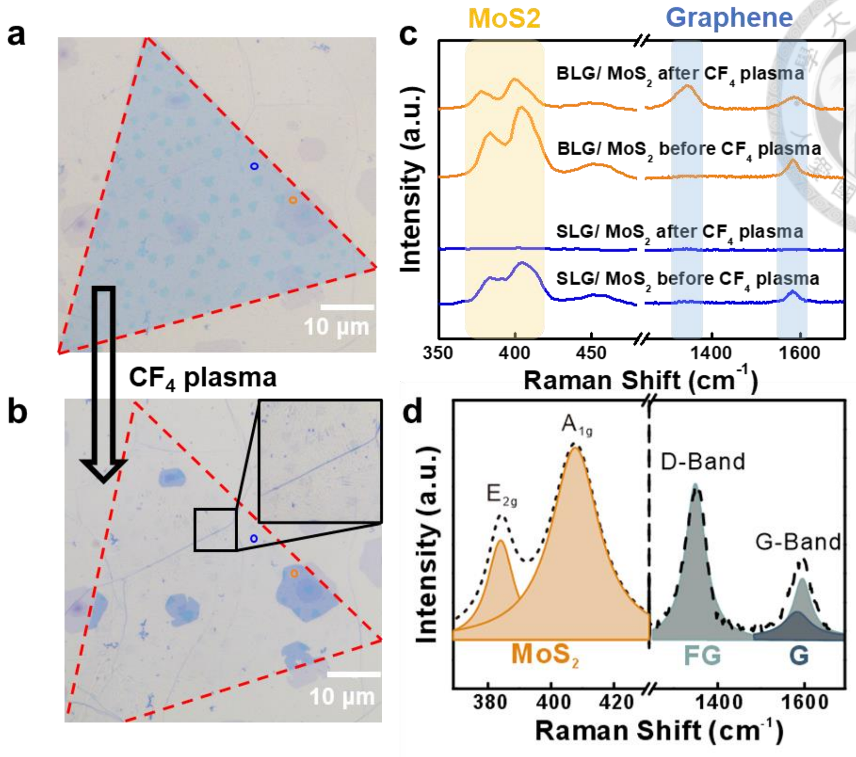

Figure 3.1-2 (a, b) Optical micrograph and (c) Raman spectra before and after patterning indicating removal of SLG regions. (d) Deconvolution of Raman features indicates the retention of all three components.

3.1.2.2 AFM

Atomic force microscopy (AFM) image (**Figure 3.1-3a**) confirmed the formation of FG/G/MoS_2 heterojunction nanoribbon arrays with high density and parallel alignment with the copper substrate's crystalline texture[99]. The average density of heterojunction nanoribbon arrays on Si/SiO_2 substrate is around 200 nm^{-1} with high aspect ratio (**Figure 3.1-3b**).

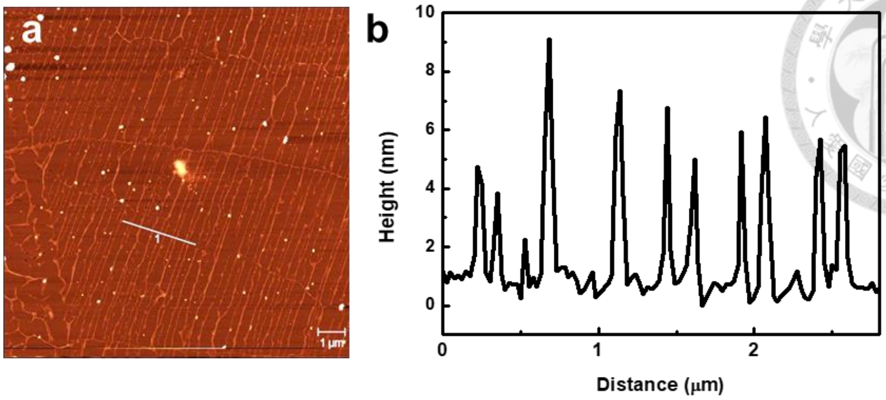

Figure 3.1-3 (a) AFM image and (b) the height of heterojunction nanoribbon on Si/SiO$_2$ substrate.

3.1.2.3 TEM and SAED

This transformation is additionally supported by TEM (**Figure 3.1-4a**) and selected area diffraction (**Figure 3.1-4b**), revealing characteristic patterns for MoS$_2$, graphene, and fluorographene. Selected-area electron diffraction (SAED) shows three sets of hexagonal diffraction patterns. One set was assigned to the (100), (110), and (200) MoS$_2$ planes with a lattice spacing of 0.273 nm, 0.160 nm, and 0.137 nm respectively, agreeing with the simulation **(Figure 3.1-4c)** and previous reports[100]. The other sets correspond to the (100) and (110) planes of the graphene and fluorographene lattice. The extracted lattice spacing of 0.213nm and 0.123 nm agrees with both lattice types[101]. The lattice misalignment is anticipated due to the random orientation of the components during wrinkle collapse and transfer.

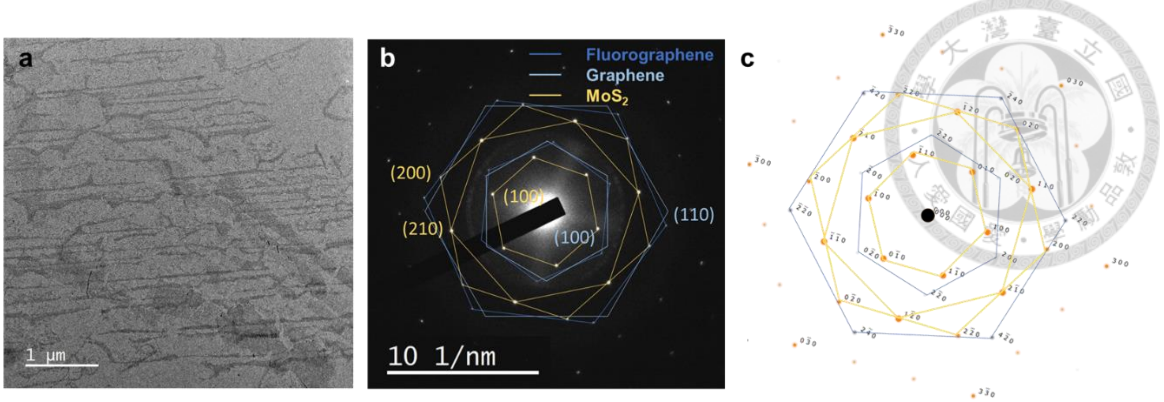

Figure 3.1-4 (a) TEM image and (b) SAED of heterojunction nanoribbon. (c) Simulated diffraction pattern by crystal maker software.

3.2 OEFs in heterojunction nanoribbons

The confinement to nanometer width imbues the heterostructure with edge-dominated electrostatics. While extended vertical 2D heterojunctions typically exhibit a one-dimensional field distribution, the discontinuous dielectric environment and the lack of charge screening are expected to result in a complex electric field pattern[102]. To validate this hypothesis, we perform finite element simulations of the electrostatics using the experimentally determined heterojunction composition. We assumed a work-function difference of 0.45 eV between MoS_2[103] and fluorographene[104]. The simulation results confirm a uniform field emerging in the extended heterojunction (**Figure 3.2-1a**). The edge-dominated heterojunction, on the other hand, exhibits a complex field distribution with a pronounced fringing field at the edges **(Figure 3.2-2b)**. The resulting OEF is almost parallel to the nanoribbon edge and thus penetrates the edge/electrolyte interface. The strength of these fringing OEF reaches up to 0.7V nm^{-1} which is comparable to the built-in field of vertical heterojunctions.

To experimentally verify this prediction, we conduct spectroscopic characterization on a single heterojunction nanoribbon. Spatially resolved Raman spectroscopy demonstrates variations in Raman features within the ribbon (**Figure 3.2-1c**). To identify the presence of an OEF at the MoS_2 edge, we map out the difference in Raman shift between the A_{1g} and E_{2g} features, as they are known to be sensitive to electrostatic effects[105]. We observe a clear upshift in the characteristic peak difference, indicating enhanced hole accumulation at the edges (**Figure 3.2-1d**). A similar trend is also observed for the graphene G-band position, supporting the formation of a lateral dipole between the nanoribbon center and its edge.

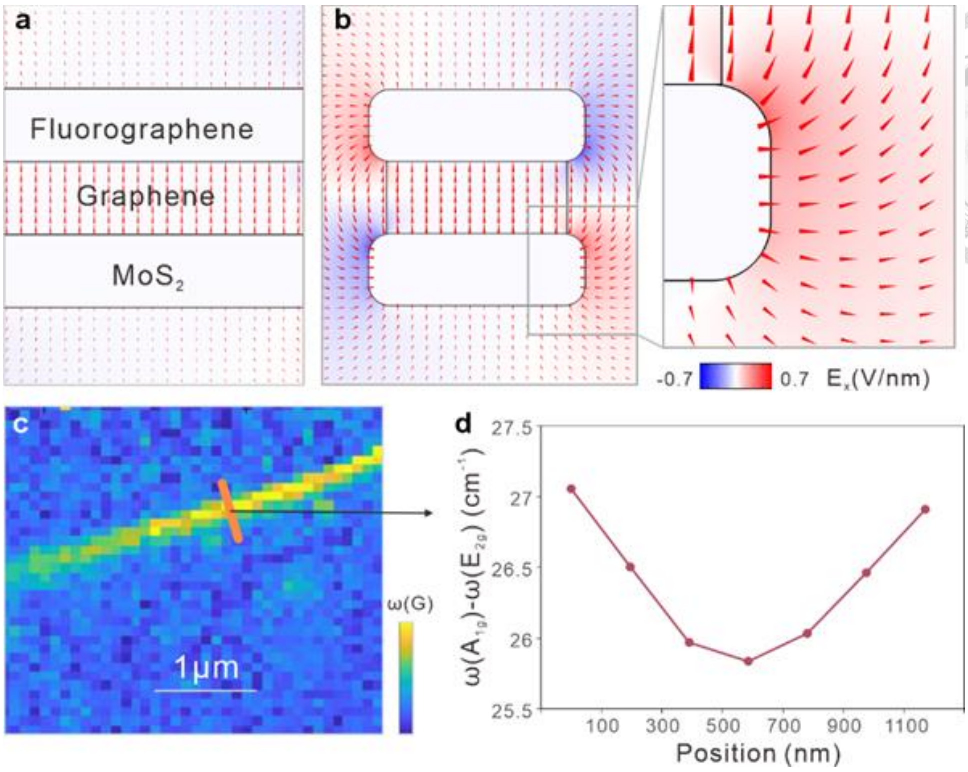

Figure 3.2-1 Finite element simulation of electric fields in MoS_2/graphene/fluorographene heterojunction, (a) for a laterally extended 2D vertical heterojunction, (b) for a heterojunction nanoribbon. (c) Raman mapping of G-Band intensity of a single nanoribbon. (d) Raman peak shift between E_{2g} and A_{1g} across the nanoribbon as indicated in (c).

3.3 Electrochemical performance of OEF-enhanced edges

■Setup for electrochemical measurement

We evaluate the impact of the observed fringing fields on the electrochemical performance of MoS_2 edges. For this purpose, we fabricate a microelectrode cell that permits contact with multiple nanoribbons in parallel (**Figure 3.3-1**). Photolithography was utilized to open a window in a photoresist layer that protects the metal electrode

doi:10.6342/NTU202402275

and exposes only a 50μm × 50μm large area of the nanoribbon array to ensure the HER performance is all contribution from the material.

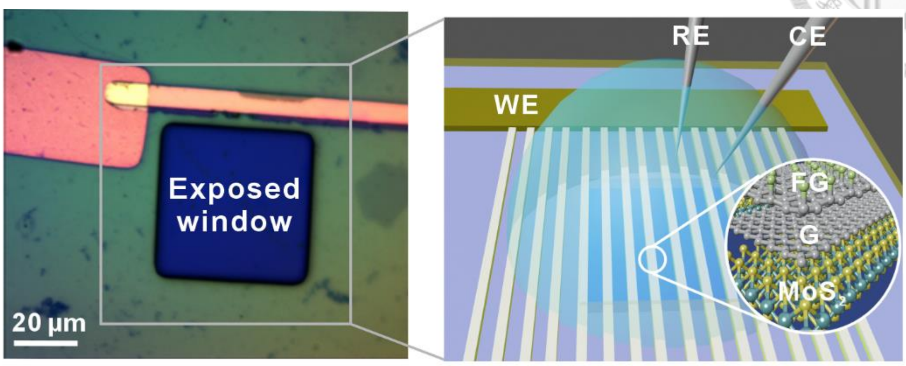

Figure 3.3-1 The schematic illustration and optical micrograph of heterojunction nanoribbon with a reaction window and gold electrode for electrochemical measurement.

Electrochemical impedance spectroscopy (EIS)

Electrochemical impedance spectroscopy (EIS) was conducted to evaluate the heterogeneous charge transfer kinetics at the edge **(Figure 3a)**. The observed large semicircle in the Nyquist plot, with negligible separation from the origin, indicates that the electrochemical reaction is limited by a heterogeneous charge transfer step rather than by the uncompensated resistance of carrier conduction within the heterostructure or the electrolyte[106].

Fits to an equivalent circuit allow for quantification of this observation. We approximate the setup with an electrolyte resistance and a series RC circuit, which represents the charge transfer at the edge/electrolyte interface (inset in **Figure 3b**). A decrease in charge transfer resistance by one order of magnitude is observed as the continuous film is patterned into a nanoribbon array, consistent with previous reports.[107] However, this enhancement is surpassed by edge OEF and the heterogeneous charge transfer resistance decreases by two orders of magnitude compared to pristine edges.

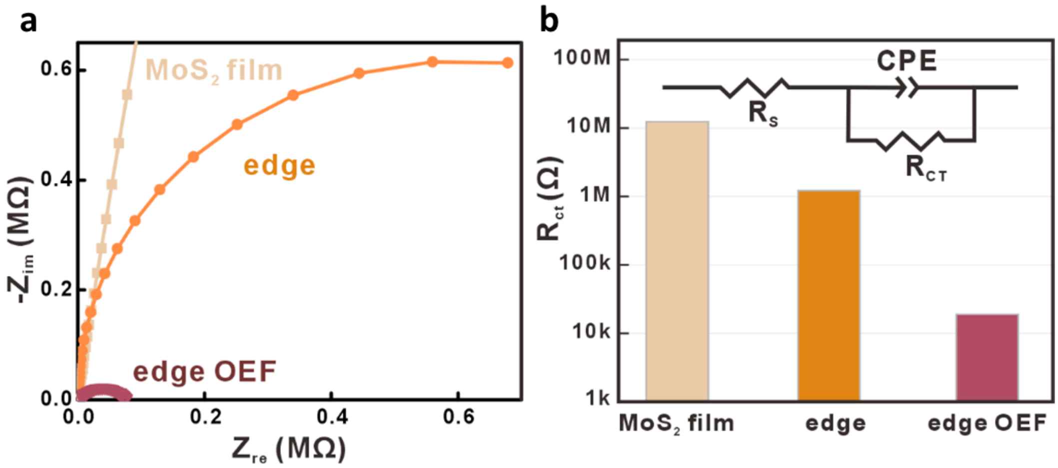

Figure 3.3-2 (a) Nyquist impedances and (b) charge transfer resistance of MoS_2 flake, MoS_2 nanoribbon, and heterojunction nanoribbon.

3.4 Ab-initio simulation

To understand the OEF-enhancement mechanism on 2D materials edges, we conduct ab-initio simulations on the hydrogen evolution reaction due to its conceptual simplicity and impact on sustainable energy generation. We focus on the Mo-rich edge of MoS_2, given its established electrochemical activity for hydrogen evolution reaction.[108, 109] To optimize HER activity, the binding energy to adsorbed hydrogen should be finely balanced. A strong bond is challenging for H atom to break during desorption, while, in

doi:10.6342/NTU202402275

contrast, a weak bond is difficult for H atom to adsorb on the active sites. Among all the edges and basal plane of FG/G/MoS_2 nanoribbon, the ΔG_H^* of Mo edge (-0.36 eV) shows significantly better HER activity than fluorographene (-3.14 eV) and graphene edge (-3.27 eV) (**Figure 3.4-1**), indicating that the Mo edge of MoS_2 plays a dominant role in the reaction within FG/G/MoS_2 nanoribbon.

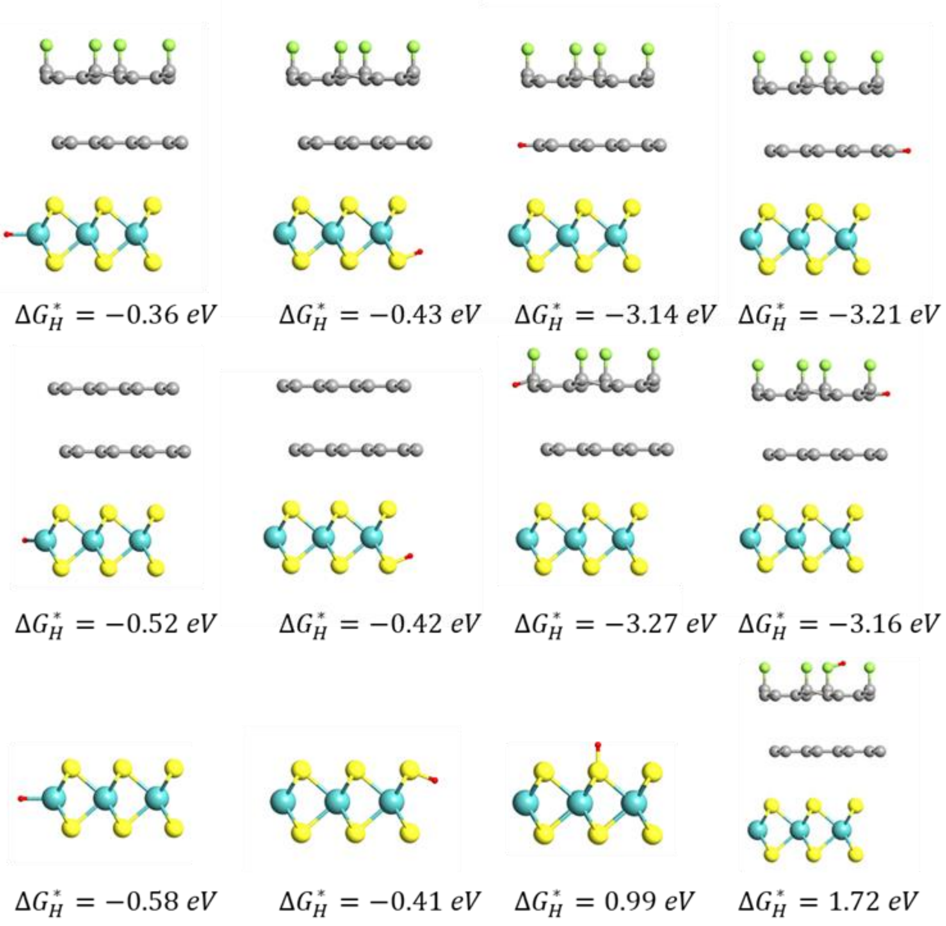

Figure 3.4-1 ΔG_H^* at different adsorption sites of MoS_2 nanoribbon and heterostructure nanoribbon. Elements: blue, Mo; yellow, S; green, F; red, H.

Furthermore, the pristine MoS_2 edge was compared to the edge within the heterojunction nanoribbon composed of MoS_2/graphene/fluorographene. **(Figure 3.4-**

2a and 3.4-2b). Adsorption of a hydrogen atom results in a charge redistribution within the MoS_2 due to the difference in electron affinity **(Figure 3.4-2c)**. When investigating the charge distribution at each row of Mo atoms within the nanoribbon, the impact of the edge OEF can be seen. Compared to the near-constant charge distribution within a pristine nanoribbon, the edge-OEF shows a decrease in charge close to the adsorbed hydrogen **(Figure 3.4-2d)**. The Mo atom neighboring the proton lowers its charge by $0.47e^-$ suggesting a significant effect of OEFs on the interaction between reactants.

The suitability of a catalyst for the hydrogen evolution reaction (HER) is quantified by the Gibbs free energy of hydrogen adsorption (ΔG_H^*). A negative ΔG_H^* indicates a strong bond, making it difficult for the hydrogen atom to desorb, while a positive ΔGH* represents a weak bond, limiting adsorption. Consequently, a ΔG_H^* value close to 0 represents the optimal balance between adsorption and desorption. Pristine MoS2 edges exhibit a ΔG_H^* of -0.58 eV, consistent with previous reports, indicating a desorption-limited reaction process. The charge redistribution facilitated by F^2E^3 simplifies desorption, resulting in a ΔG_H^* of -0.36 eV **(Figure 3.4-2e)**. While the employed PBE functional is known to overestimate the absolute value of the hydrogen adsorption energy [110, 111], the observed trend toward the optimal adsorption energy indicates the impact of edge OEFs on electrochemical reactions.

doi:10.6342/NTU202402275

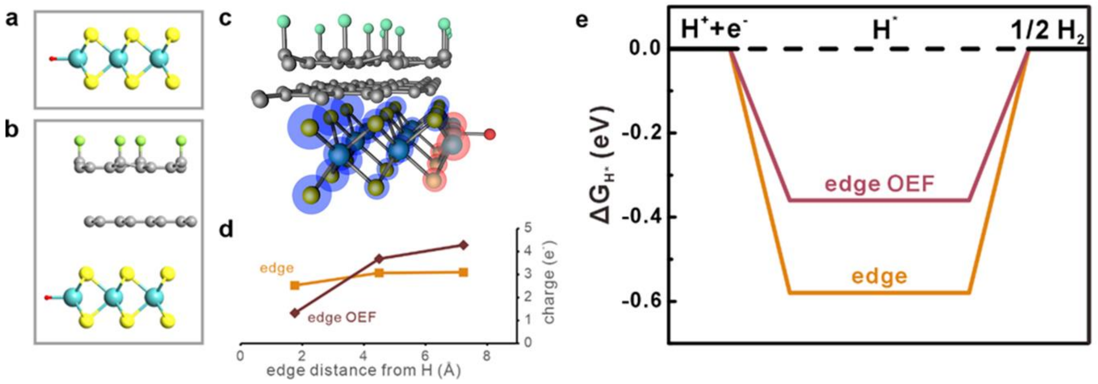

Figure 3.4-2 (a) Side view of supercell model of MoS_2 nanoribbon, and (b) heterojunction nanoribbon bonded with hydrogen. Elements: blue, Mo; yellow, S; green, F; red, H. (c) Difference in Bader charge between MoS_2 nanoribbon and nanoribbon heterostructure. The blue and red spheres are proportional to the charge accumulation and depletion, respectively. (d) Bader charge analysis for rows of Mo atoms parallel to the edge of the MoS_2 nanoribbon in the pristine and OEF case. (e) Gibbs Free Energy $\Delta G_H{}^*$ vs. reaction coordinates for hydrogen adsorption on Mo edge for pristine and heterojunction conditions.

3.5 HER performance of OEF-enhanced edges

■Polarization curve

We confirm these predictions by conducting experimental HER. We first measure the typical polarization curve in acidic solution **(Figure 3.5-1)**. To permit comparison, the reaction current at a given potential was normalized by the basal plane area as detailed in the supplementary material. As predicted, the MoS_2 flake exhibited the poorest HER performance in agreement with the EIS results, confirming the limited catalytic activity of the MoS_2 basal plane[96]. The formation of edges enhances the HER performance, as expected. The importance of OEFs is demonstrated by the significant increase in exchange current density in the HER polarogram **(Figure 3.5-1)**.

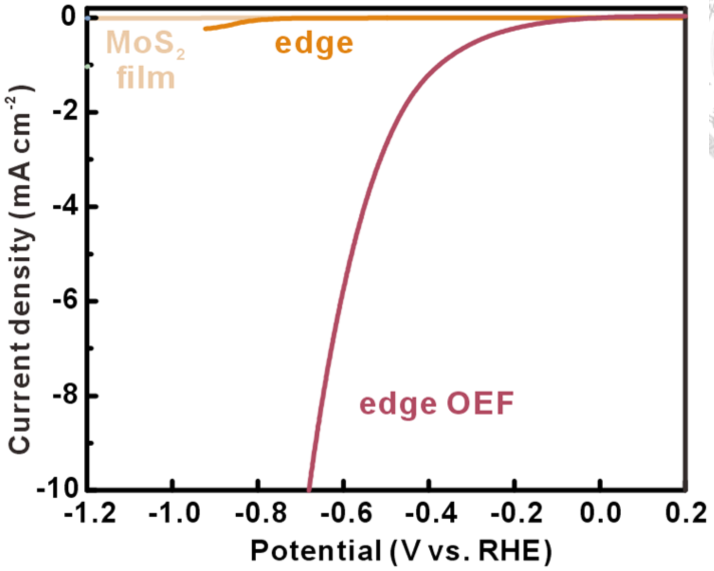

Figure 3.5-1 Polarization curves MoS$_2$ film, MoS$_2$ nanoribbon, and heterojunction nanoribbon.

Tafel slope

To quantify the kinetics of the HER process, we extract the Tafel slope **(Figure 3.5-2)**. Recent work has demonstrated that this feature not only allows the extraction of the rate-determining step during HER but also provides information about the material's properties. Analysis of the uncompensated resistance reveals restrictions to carrier transport within the electrode[89]. We performed iR correction on the polarization curves, and the Tafel slope with iR correction was obtained **(Figure 3.5-2)**. The original voltage was adjusted by subtracting the voltage contributed from the solution resistance (R_s) and uncompensated resistance ($R\mu$). We find that the Tafel slope after iR correction is reduced, indicating the importance of accounting for the potential drop across the nanoribbon. The reduction was more substantial for the pristine nanoribbon than for the

OEF-enhanced nanoribbon, indicating the synergy of the components in enhancing the conduction. The small impact on the electrochemical parameters, however, demonstrates the controlling effect of OEFs over other heterojunction parameters. The corrected Tafel slope approaches 69 mV dec^{-1} and a sample-to-sample variability of 7% was observed.

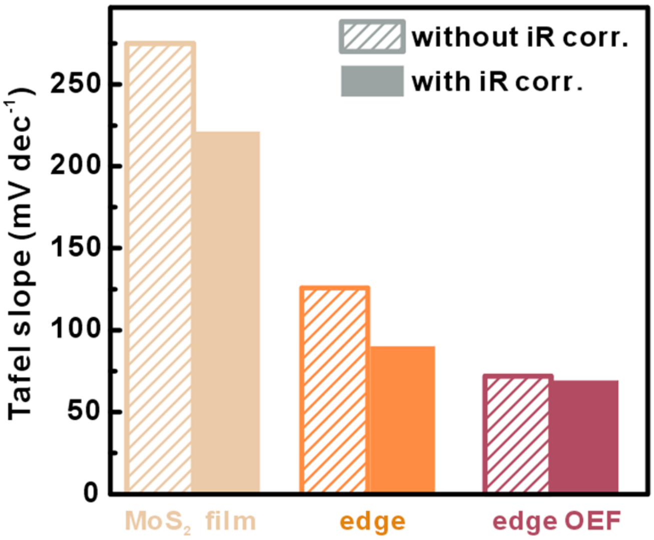

Figure 3.5-2 Tafel slopes with and without iR correction.

■Comparison of literature

The extracted reaction current density represents the lower boundary, as it underestimates the contribution of the edge but the extracted value is among the highest reported values for 2D materials-based HER catalysts as detailed in **Table T1**. Future efforts could further enhance the performance by increasing the density of nanoribbons within the array[107].

doi:10.6342/NTU202402275

Finally, the turnover frequency is a quantitative measure of how quickly a catalyst can facilitate a specific reaction per unit time, following the methodology outlined in a previous study by Jaramillo et al.[107] (**more details in Table T1**) we observe a tripling in TOF between pristine and heterostructure edges with the highest TOF reaching 7.23 s^{-1}. The combination of low Tafel slope and high turnover frequency demonstrates the impact of OEFs toward HER **(Figure 3.5-3, see Table T1 for a comparison to references).** Future work could further enhance this performance by utilizing heterojunction components with larger differences in work function.

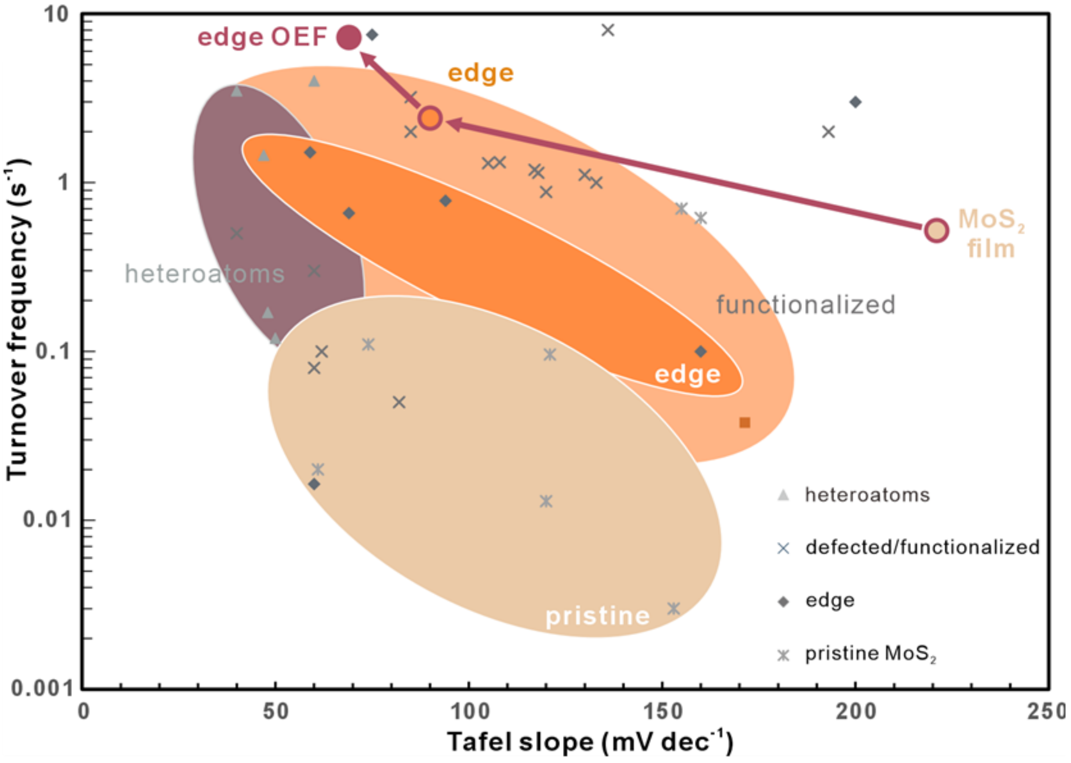

Figure 3.5-3 Comparison of literature values of Tafel slope versus TOF to our results (more details, including comparison of reaction current density, are provided in **Table T1**).

doi:10.6342/NTU202402275

Table T1. Comparison of Tafel slope, turnover frequency (TOF), and current density for our work with references

Materials type	Tafel slope (mV dec^{-1})	TOF (s^{-1})	Current density @-200mV (mA cm^{-2})	Ref.
pristine MoS$_2$	**221**	**0.52**	**3.5×10^{-4}**	**Our work**
pristine MoS$_2$	120	0.013	0.096	[112]
pristine MoS$_2$	61	0.02	>100	[113]
pristine MoS$_2$	121	0.096	6.8	[114]
pristine MoS$_2$	74	0.11	53	[115]
pristine MoS$_2$	153	3.00×10^{-3}	8.37×10^{-4}	[107]
pristine MoS$_2$	160	0.617	0.6	[116]
pristine MoS$_2$	155	0.7	4.46	[91]
pristine MoS$_2$ (edge)	**90**	**2.41**	**1.4×10^{-3}**	**Our Work**
OEF MoS$_2$ edge	**69**	**7.23**	**0.551**	**Our Work**
pristine MoS$_2$ (edge)	160	0.1	>10	[117]
pristine MoS$_2$ (edge)	69	0.66	52.9	[114]
pristine MoS$_2$ (edge)	94	0.78	1.3×10^{-3}	[107]
pristine MoS$_2$ (edge)	59	1.51	152.9	[114]
pristine MoS$_2$ (edge)	60	1.64×10^{-2}	>0.3	[49]
pristine MoS$_2$ (edge)	200	3	6×10^{-3}	[109]
pristine MoS$_2$ (edge)	75	7.5	12.4	[118]
other catalyst (Hg)	-	1.04×10^{-9}	-	[49]
other catalyst (2H-WS$_2$)	-	0.078	5	[119]

other catalyst (Mo_2C)	63	-	56	[113]
other catalyst (MoSe)	118	0.014	0.11	[112]
other catalyst (MoP)	50	0.024	>120	[120]
other catalyst (Pt)	87	0.32	>40	[121]
other catalyst (Ru)	107	0.04	>40	[121]
other catalyst (c-$RuSe_2$)	130	0.07	40	[121]
other catalyst ($[Mo_3S_4]^{4+}$)	120	0.07	5~10	[122]
other catalyst (Fe-CoS_2)	73	0.17	>60	[123]
other catalyst (CoS_2)	90	0.17	>60	[123]
other catalyst (Pt/C)	30	0.28	>60	[124]
other catalyst (h-$RuSe_2$)	95	0.34	>40	[121]
other catalyst (P-CoS_2)	57	0.55	>60	[123]
other catalyst (C-Ir NSs)	36	0.6	>90	[125]
other catalyst (Fe/P-CoS_2)	56	1.33	>60	[123]
other catalyst (AC-Ir NS)	27	3.6	>90	[125]
other catalyst (Ru/NC)	17	8.9	>60	[124]
defected/functionalized MoS_2	82	0.05	3	[126]
defected/functionalized MoS_2	60	0.08	16	[126]
defected/functionalized MoS_2	62	0.1	200	[127]
defected/functionalized MoS_2	60	0.3	13	[128]
defected/functionalized MoS_2	40	0.5	5.97	[129]
defected/functionalized MoS_2	120	0.88	-	[116]
defected/functionalized MoS_2	133	1	0.32	[116]
defected/functionalized MoS_2	130	1.11	0.6	[116]
defected/functionalized MoS_2	118	1.14	0.6	[116]

defected/functionalized MoS_2	117	1.19	0.6	[116]
defected/functionalized MoS_2	105	1.3	0.65	[116]
defected/functionalized MoS_2	108	1.32	0.6	[116]
defected/functionalized MoS_2	85	2	1.19	[130]
defected/functionalized MoS_2	193	2	0.38	[131]
defected/functionalized MoS_2	85	3.2	-	[117]
defected/functionalized MoS_2	136	8	0.039	[109]
combination of materials	48	0.17	>100	[113]
combination of materials	47	1.45	0.1~1	[132]
combination of materials	40	3.5	>25	[133]
combination of materials	60	4	1.05	[134]
combination of materials	50	0.12	>120	[120]

doi:10.6342/NTU202402275

Chapter 4 Conclusion

We have demonstrated the OEF-induced enhancement of 2D materials edge-based electrochemistry. Through a powerful and universal bottom-up patterning approach, heterojunction nanoribbons were produced that exhibit complex ternary composition and nanometer width. The resulting edge-dominated electrochemical characteristics exhibit significant differences in electrochemical performance compared to bare nanoribbons. Spectroscopic characterization and ab-initio simulations demonstrate the formation of an oriented electric field that modifies the charge transfer dynamics at the edge/electrolyte interface. The advantage of our universally applicable edge OEF approach was demonstrated by a 30% decrease in Tafel slope and superior turnover frequency over previous 2D materials-based HER catalysts. Our results open up a new route toward optimizing the reactivity of catalysts by tailoring their reactant's adsorption geometry.

Reference

1. Novoselov, K.S., et al., *Two-dimensional gas of massless Dirac fermions in graphene.* nature, 2005. **438**(7065): p. 197-200.
2. Chhowalla, M., et al., *The chemistry of two-dimensional layered transition metal dichalcogenide nanosheets.* Nature Chemistry, 2013. **5**(4): p. 263-275.
3. Zhou, J., et al., *A library of atomically thin metal chalcogenides.* Nature, 2018. **556**(7701): p. 355-359.
4. Xu, J., J. Zhang, W. Zhang, and C.S. Lee, *Interlayer nanoarchitectonics of two-dimensional transition-metal dichalcogenides nanosheets for energy storage and conversion applications.* Advanced Energy Materials, 2017. **7**(23): p. 1700571.
5. Zhi, C., et al., *Large-scale fabrication of boron nitride nanosheets and their utilization in polymeric composites with improved thermal and mechanical properties.* Advanced materials, 2009. **21**(28): p. 2889-2893.
6. Hanlon, D., et al., *Production of molybdenum trioxide nanosheets by liquid exfoliation and their application in high-performance supercapacitors.* Chemistry of Materials, 2014. **26**(4): p. 1751-1763.
7. Xiao, X., et al., *Scalable salt-templated synthesis of two-dimensional transition metal oxides.* Nature Communications, 2016. **7**(1): p. 11296.
8. Li, Z., et al., *Synthesis and thermal stability of two-dimensional carbide MXene* Ti_3C_2. Materials Science and Engineering: B, 2015. **191**: p. 33-40.
9. Seh, Z.W., et al., *Two-dimensional molybdenum carbide (MXene) as an efficient electrocatalyst for hydrogen evolution.* ACS Energy Letters, 2016. **1**(3): p. 589-594.
10. Urbankowski, P., et al., *Synthesis of two-dimensional titanium nitride* Ti_4N_3 *(MXene).* Nanoscale, 2016. **8**(22): p. 11385-11391.
11. Geim, A.K. and I.V. Grigorieva, *Van der Waals heterostructures.* Nature, 2013. **499**(7459): p. 419-425.
12. Bolotin, K.I., et al., *Ultrahigh electron mobility in suspended graphene.* Solid state communications, 2008. **146**(9-10): p. 351-355.
13. Lee, C., X. Wei, J.W. Kysar, and J. Hone, *Measurement of the elastic properties and intrinsic strength of monolayer graphene.* science, 2008. **321**(5887): p. 385-388.
14. Balandin, A.A., et al., *Superior thermal conductivity of single-layer graphene.* Nano letters, 2008. **8**(3): p. 902-907.

doi:10.6342/NTU202402275

15. Zhu, Y., et al., *Graphene and graphene oxide: synthesis, properties, and applications.* Advanced materials, 2010. **22**(35): p. 3906-3924.
16. Avouris, P. and F. Xia, *Graphene applications in electronics and photonics.* Mrs Bulletin, 2012. **37**(12): p. 1225-1234.
17. Jo, G., et al., *The application of graphene as electrodes in electrical and optical devices.* Nanotechnology, 2012. **23**(11): p. 112001.
18. Olabi, A.G., M.A. Abdelkareem, T. Wilberforce, and E.T. Sayed, *Application of graphene in energy storage device–A review.* Renewable and Sustainable Energy Reviews, 2021. **135**: p. 110026.
19. Nguyen, B.H. and V.H. Nguyen, *Promising applications of graphene and graphene-based nanostructures.* Advances in Natural Sciences: Nanoscience and Nanotechnology, 2016. **7**(2): p. 023002.
20. Li, X., et al., *Graphene in photocatalysis: a review.* Small, 2016. **12**(48): p. 6640-6696.
21. Zhang, L., et al., *Photo-induced free radical modification of graphene.* Small, 2013. **9**(8): p. 1134-1143.
22. Liao, L., H. Peng, and Z. Liu, *Chemistry makes graphene beyond graphene.* Journal of the American Chemical Society, 2014. **136**(35): p. 12194-12200.
23. Gao, X., et al., *Opening a large band gap for graphene by covalent addition.* Chemical Physics Letters, 2013. **555**: p. 1-6.
24. Zhang, Y., et al., *Direct observation of a widely tunable bandgap in bilayer graphene.* Nature, 2009. **459**(7248): p. 820-823.
25. Nair, R.R., et al., *Fluorographene: a two-dimensional counterpart of Teflon.* small, 2010. **6**(24): p. 2877-2884.
26. Baraket, M., et al., *The functionalization of graphene using electron-beam generated plasmas.* Applied Physics Letters, 2010. **96**(23).
27. Bon, S.B., et al., *Plasma fluorination of chemically derived graphene sheets and subsequent modification with butylamine.* Chemistry of Materials, 2009. **21**(14): p. 3433-3438.
28. Gao, X. and X.S. Tang, *Effective reduction of graphene oxide thin films by a fluorinating agent: diethylaminosulfur trifluoride.* Carbon, 2014. **76**: p. 133-140.
29. Lee, W.H., et al., *Selective-area fluorination of graphene with fluoropolymer and laser irradiation.* Nano letters, 2012. **12**(5): p. 2374-2378.
30. Bruna, M., et al., *Synthesis and properties of monolayer graphene oxyfluoride.* Journal of Materials Chemistry, 2011. **21**(46): p. 18730-18737.
31. Romero-Aburto, R., et al., *Fluorinated graphene oxide; a new multimodal material for biological applications.* Advanced materials (Deerfield Beach, Fla.), 2013. **25**(39): p. 5632.

doi:10.6342/NTU202402275

32. Dubois, M., et al., *Thermal exfoliation of fluorinated graphite.* Carbon, 2014. **77**: p. 688-704.
33. Robinson, J.T., et al., *Properties of fluorinated graphene films.* Nano letters, 2010. **10**(8): p. 3001-3005.
34. Chen, S.H., M. Hofmann, Z.L. Yen, and Y.P. Hsieh, *2D Material Enabled Offset-Patterning with Atomic Resolution.* Advanced Functional Materials, 2020. **30**(40): p. 2004370.
35. Han, G.H., et al., *van der Waals metallic transition metal dichalcogenides.* Chemical Reviews, 2018. **118**(13): p. 6297-6336.
36. Choi, W., et al., *Recent development of two-dimensional transition metal dichalcogenides and their applications.* Materials Today, 2017. **20**(3): p. 116-130.
37. Xia, F., et al., *Two-dimensional material nanophotonics.* Nature Photonics, 2014. **8**(12): p. 899-907.
38. Del Pozo-Zamudio, O., et al., *Photoluminescence of two-dimensional GaTe and GaSe films.* 2D Materials, 2015. **2**(3): p. 035010.
39. Tongay, S., et al., *Monolayer behavior in bulk* ReS_2 *due to electronic and vibrational decoupling.* Nature Communications, 2014. **5**(1): p. 3252.
40. Das, S., H.-Y. Chen, A.V. Penumatcha, and J. Appenzeller, *High-performance multilayer* MoS_2 *transistors with scandium contacts.* Nano letters, 2013. **13**(1): p. 100-105.
41. Lee, G.-H., et al., *Highly stable, dual-gated* MoS_2 *transistors encapsulated by hexagonal boron nitride with gate-controllable contact, resistance, and threshold voltage.* ACS Nano, 2015. **9**(7): p. 7019-7026.
42. Castellanos-Gomez, A., et al., *Elastic properties of freely suspended* MoS_2 *nanosheets.* arXiv preprint arXiv:1202.4439, 2012.
43. Bertolazzi, S., J. Brivio, and A. Kis, *Stretching and breaking of ultrathin* MoS_2*.* ACS Nano, 2011. **5**(12): p. 9703-9709.
44. Novoselov, K.S., A. Mishchenko, A. Carvalho, and A. Castro Neto, *2D materials and van der Waals heterostructures.* Science, 2016. **353**(6298): p. aac9439.
45. Liu, Y., et al., *Van der Waals heterostructures and devices.* Nature Reviews Materials, 2016. **1**(9): p. 1-17.
46. Zou, X. and Y. Zhang, *Noble metal-free hydrogen evolution catalysts for water splitting.* Chemical Society Reviews, 2015. **44**(15): p. 5148-5180.
47. McKone, J.R., et al., *Earth-abundant hydrogen evolution electrocatalysts.* Chemical Science, 2014. **5**(3): p. 865-878.
48. Lasia, A., *Mechanism and kinetics of the hydrogen evolution reaction.*

doi:10.6342/NTU202402275

international journal of hydrogen energy, 2019. **44**(36): p. 19484-19518.

49. Conway, B. and B. Tilak, *Interfacial processes involving electrocatalytic evolution and oxidation of* H_2*, and the role of chemisorbed H.* Electrochimica Acta, 2002. **47**(22-23): p. 3571-3594.

50. Luo, Y., et al., *Transition-metal dichalcogenides/*$Mg (OH)_2$ *van der Waals heterostructures as promising water-splitting photocatalysts: a first-principles study.* Physical Chemistry Chemical Physics, 2019. **21**(4): p. 1791-1796.

51. Luo, Y., et al., *First-principles study on transition-metal dichalcogenide/BSe van der Waals heterostructures: a promising water-splitting photocatalyst.* The Journal of Physical Chemistry C, 2019. **123**(37): p. 22742-22751.

52. Wei, Y., R.A. Soomro, X. Xie, and B. Xu, *Design of efficient electrocatalysts for hydrogen evolution reaction based on 2D MXenes.* Journal of Energy Chemistry, 2021. **55**: p. 244-255.

53. Zhu, K., et al., *Two-dimensional transition-metal dichalcogenides for electrochemical hydrogen evolution reaction.* FlatChem, 2019. **18**: p. 100140.

54. Chen, Z., et al., *Metal-organic framework-derived nanocomposites for electrocatalytic hydrogen evolution reaction.* Progress in Materials Science, 2020. **108**: p. 100618.

55. Yan, H., et al., *Holey reduced graphene oxide coupled with an* $Mo_2N–Mo_2C$ *heterojunction for efficient hydrogen evolution.* Advanced Materials, 2018. **30**(2): p. 1704156.

56. Sabatier, P., *Hydrogénations et déshydrogénations par catalyse.* Berichte der deutschen chemischen Gesellschaft, 1911. **44**(3): p. 1984-2001.

57. Mahmood, N., et al., *Electrocatalysts for hydrogen evolution in alkaline electrolytes: mechanisms, challenges, and prospective solutions.* Advanced science, 2018. **5**(2): p. 1700464.

58. Nørskov, J.K., et al., *Trends in the exchange current for hydrogen evolution.* Journal of The Electrochemical Society, 2005. **152**(3): p. J23.

59. Jaramillo, T.F., et al., *Identification of active edge sites for electrochemical* H_2 *evolution from* MoS_2 *nanocatalysts.* science, 2007. **317**(5834): p. 100-102.

60. Seh, Z.W., et al., *Combining theory and experiment in electrocatalysis: Insights into materials design.* Science, 2017. **355**(6321).

61. Hua, W., H.-H. Sun, F. Xu, and J.-G. Wang, *A review and perspective on molybdenum-based electrocatalysts for hydrogen evolution reaction.* Rare Metals, 2020. **39**(4): p. 335-351.

62. Voiry, D., H.S. Shin, K.P. Loh, and M. Chhowalla, *Low-dimensional catalysts for hydrogen evolution and* CO_2 *reduction.* Nature Reviews Chemistry, 2018. **2**(1): p. 0105.

63. Wang, Z. and B. Mi, *Environmental Applications of 2D Molybdenum Disulfide (MoS(2)) Nanosheets.* Environ Sci Technol, 2017. **51**(15): p. 8229-8244.
64. Han, S.W., et al., *Hydrogen interaction with selectively desulfurized MoS_2 surface using Ne^+ sputtering.* Journal of Applied Physics, 2019. **125**(8).
65. Xie, J., et al., *Defect-rich MoS_2 ultrathin nanosheets with additional active edge sites for enhanced electrocatalytic hydrogen evolution.* Advanced Materials, 2013(40): p. 5807-5813.
66. Xie, J., et al., *Controllable disorder engineering in oxygen-incorporated MoS_2 ultrathin nanosheets for efficient hydrogen evolution.* J Am Chem Soc, 2013. **135**(47): p. 17881-8.
67. Cao, Y., *Roadmap and Direction toward High-Performance MoS_2 Hydrogen Evolution Catalysts.* ACS Nano, 2021. **15**(7): p. 11014-11039.
68. Xie, J., et al., *Defect-rich MoS2 ultrathin nanosheets with additional active edge sites for enhanced electrocatalytic hydrogen evolution.* Advanced Materials, 2013. **25**(40): p. 5807-5813.
69. Li, H., et al., *Corrigendum: Activating and optimizing MoS_2 basal planes for hydrogen evolution through the formation of strained sulfur vacancies.* Nat Mater, 2016. **15**(3): p. 364.
70. He, Y., et al., *Engineering grain boundaries at the 2D limit for the hydrogen evolution reaction.* Nat Commun, 2020. **11**(1): p. 57.
71. Kong, D., et al., *Synthesis of MoS_2 and $MoSe_2$ films with vertically aligned layers.* Nano Lett, 2013. **13**(3): p. 1341-7.
72. Yu, X., et al., *Design of MoS_2/Graphene van der Waals Heterostructure as Highly Efficient and Stable Electrocatalyst for Hydrogen Evolution in Acidic and Alkaline Media.* ACS Appl Mater Interfaces, 2020. **12**(22): p. 24777-24785.
73. Li, Y., et al., *MoS_2 nanoparticles grown on graphene: an advanced catalyst for the hydrogen evolution reaction.* J Am Chem Soc, 2011. **133**(19): p. 7296-9.
74. Shen, W., et al., *Rhodium Nanoparticles/F-Doped Graphene Composites as Multifunctional Electrocatalyst Superior to Pt/C for Hydrogen Evolution and Formic Acid Oxidation Reaction.* ACS Appl Mater Interfaces, 2018. **10**(39): p. 33153-33161.
75. Singh, D. and R. Ahuja, *Theoretical prediction of a Bi-Doped β-Antimonene monolayer as a highly efficient photocatalyst for oxygen reduction and overall water splitting.* ACS applied materials & interfaces, 2021. **13**(47): p. 56254-56264.
76. Cao, Y., *Roadmap and direction toward high-performance MoS_2 hydrogen evolution catalysts.* ACS Nano, 2021. **15**(7): p. 11014-11039.
77. Shaik, S., et al., *Electric-field mediated chemistry: uncovering and exploiting*

the potential of (oriented) electric fields to exert chemical catalysis and reaction control. Journal of the American Chemical Society, 2020. **142**(29): p. 12551-12562.

78. Shaik, S., D. Mandal, and R. Ramanan, *Oriented electric fields as future smart reagents in chemistry.* Nature Chemistry, 2016. **8**(12): p. 1091-1098.

79. Pan, X., et al., *Electric-field-assisted proton coupling enhanced oxygen evolution reaction.* Nature Communications, 2024. **15**(1): p. 3354.

80. Aragones, A.C., et al., *Electrostatic catalysis of a Diels–Alder reaction.* Nature, 2016. **531**(7592): p. 88-91.

81. Wang, J., et al., *Growing highly pure semiconducting carbon nanotubes by electrotwisting the helicity.* Nature Catalysis, 2018. **1**(5): p. 326-331.

82. Liu, M., et al., *Enhanced electrocatalytic CO_2 reduction via field-induced reagent concentration.* Nature, 2016. **537**(7620): p. 382-386.

83. Pecina, O. and W. Schmickler, *A model for electrochemical proton-transfer reactions.* Chemical physics, 1998. **228**(1-3): p. 265-277.

84. Cai, C., et al., *Atomically local electric field induced interface water reorientation for alkaline hydrogen evolution reaction.* Angewandte Chemie International Edition, 2023. **62**(26): p. e202300873.

85. Daiyan, R., I. MacGill, and R. Amal, *Opportunities and challenges for renewable power-to-X.* 2020, ACS Publications.

86. Seh, Z.W., et al., *Combining theory and experiment in electrocatalysis: Insights into materials design.* Science, 2017. **355**(6321): p. eaad4998.

87. Hua, W., H.-H. Sun, F. Xu, and J.-G. Wang, *A review and perspective on molybdenum-based electrocatalysts for hydrogen evolution reaction.* Rare Metals, 2020. **39**: p. 335-351.

88. Wang, Z. and B. Mi, *Environmental applications of 2D molybdenum disulfide (MoS_2) nanosheets.* Environmental science & technology, 2017. **51**(15): p. 8229-8244.

89. Muthu, J., et al., *The HER performance of 2D materials is underestimated without morphology correction.* Chemical Engineering Journal, 2023. **465**: p. 142852.

90. Huang, X., et al., *Electric field–induced selective catalysis of single-molecule reaction.* Science Advances, 2019. **5**(6): p. eaaw3072.

91. Wang, Y., S. Udyavara, M. Neurock, and C.D. Frisbie, *Field effect modulation of electrocatalytic hydrogen evolution at back-gated two-dimensional MoS_2 electrodes.* Nano letters, 2019. **19**(9): p. 6118-6123.

92. Zhang, W., et al., *Superior hydrogen evolution reaction performance in 2H-MoS_2 to that of 1T phase.* Small, 2019. **15**(31): p. 1900964.

93. Xu, J., et al., *Atomic-level polarization in electric fields of defects for electrocatalysis.* Nature Communications, 2023. **14**(1): p. 7849.

94. Zhu, J., et al., *Surface passivation for highly active, selective, stable, and scalable* CO_2 *electroreduction.* Nature Communications, 2023. **14**(1): p. 4670.

95. Raman, R., et al., *Selective activation of* MoS_2 *grain boundaries for enhanced electrochemical activity.* Nanoscale Horizons, 2024.

96. Raman, R., et al., *Selective activation of* MoS_2 *grain boundaries for enhanced electrochemical activity.* Nanoscale Horizons, 2024. **9**(6): p. 946-955.

97. Seydou, M., et al., *A DFT-D study of hydrogen adsorption on functionalized graphene.* RSC Advances, 2015. **5**(19): p. 14400-14406.

98. Fu, S., et al., *The first-principles study on the graphene/*MoS_2 *heterojunction.* AIP Advances, 2020. **10**(4).

99. Pan, Z., N. Liu, L. Fu, and Z. Liu, *Wrinkle engineering: a new approach to massive graphene nanoribbon arrays.* Journal of the American Chemical Society, 2011. **133**(44): p. 17578-17581.

100. Li, B., et al., *Growth of large area few-layer or monolayer* MoS_2 *from controllable* MoO_3 *nanowire nuclei.* RSC Advances, 2014. **4**(50): p. 26407-26412.

101. Robertson, A.W. and J.H. Warner, *Hexagonal single crystal domains of few-layer graphene on copper foils.* Nano letters, 2011. **11**(3): p. 1182-1189.

102. Nipane, A., S. Jayanti, A. Borah, and J.T. Teherani, *Electrostatics of lateral pn junctions in atomically thin materials.* Journal of Applied Physics, 2017. **122**(19).

103. Choi, S., Z. Shaolin, and W. Yang, *Layer-number-dependent work function of* MoS_2 *nanoflakes.* Journal of the Korean Physical Society, 2014. **64**: p. 1550-1555.

104. An, H., et al., *Hydrothermal preparation of fluorinated graphene hydrogel for high-performance supercapacitors.* Journal of Power Sources, 2016. **312**: p. 146-155.

105. Panasci, S.E., et al., *Strain, doping, and electronic transport of large area monolayer* MoS_2 *exfoliated on gold and transferred to an insulating substrate.* ACS Applied Materials & Interfaces, 2021. **13**(26): p. 31248-31259.

106. Ghosh, R., et al., *Exciton manipulation for enhancing photoelectrochemical hydrogen evolution reaction in wrinkled 2D heterostructures.* Advanced Materials, 2023. **35**(16): p. 2210746.

107. Chen, D.-R., et al., *Edge-dominated hydrogen evolution reactions in ultra-narrow* MoS_2 *nanoribbon arrays.* Journal of Materials Chemistry A, 2023. **11**(29): p. 15802-15810.

108. He, Y., et al., *Engineering grain boundaries at the 2D limit for the hydrogen evolution reaction.* Nature Communications, 2020. **11**(1): p. 57.

109. Zhang, R., et al., *Creating fluorine-doped MoS$_2$ edge electrodes with enhanced hydrogen evolution activity.* Small Methods, 2021. **5**(11): p. 2100612.

110. Hammer, B., L.B. Hansen, and J.K. Nørskov, *Improved adsorption energetics within density-functional theory using revised Perdew-Burke-Ernzerhof functionals.* Physical Review B, 1999. **59**(11): p. 7413.

111. Stroppa, A. and G. Kresse, *The shortcomings of semi-local and hybrid functionals: what we can learn from surface science studies.* New Journal of Physics, 2008. **10**(6): p. 063020.

112. Kong, D., et al., *Synthesis of MoS$_2$ and MoSe$_2$ films with vertically aligned layers.* Nano letters, 2013. **13**(3): p. 1341-1347.

113. Zhao, Z., et al., *Vertically aligned MoS$_2$/Mo$_2$C hybrid nanosheets grown on carbon paper for efficient electrocatalytic hydrogen evolution.* ACS Catalysis, 2017. **7**(10): p. 7312-7318.

114. Hu, J., et al., *Engineering stepped edge surface structures of MoS$_2$ sheet stacks to accelerate the hydrogen evolution reaction.* Energy & Environmental Science, 2017. **10**(2): p. 593-603.

115. Guo, B., et al., *Hollow structured micro/nano MoS$_2$ spheres for high electrocatalytic activity hydrogen evolution reaction.* ACS applied materials & interfaces, 2016. **8**(8): p. 5517-5525.

116. Tao, L., et al., *Plasma-engineered MoS$_2$ thin-film as an efficient electrocatalyst for hydrogen evolution reaction.* Chemical Communications, 2015. **51**(35): p. 7470-7473.

117. Guoqing, L., et al., *All The Catalytic Active Sites of MoS$_2$ for Hydrogen Evolution.* 2016.

118. Li, G., et al., *All the catalytic active sites of MoS$_2$ for hydrogen evolution.* Journal of the American Chemical Society, 2016. **138**(51): p. 16632-16638.

119. Xie, L., et al., *WS$_2$ moiré superlattices derived from mechanical flexibility for hydrogen evolution reaction.* Nature Communications, 2021. **12**(1): p. 5070.

120. Kibsgaard, J. and T.F. Jaramillo, *Molybdenum phosphosulfide: an active, acid-stable, earth-abundant catalyst for the hydrogen evolution reaction.* Angewandte Chemie International Edition, 2014. **53**(52): p. 14433-14437.

121. Zhao, Y., et al., *Hexagonal RuSe$_2$ nanosheets for highly efficient hydrogen evolution electrocatalysis.* Angewandte Chemie, 2021. **133**(13): p. 7089-7093.

122. Jaramillo, T.F., et al., *Hydrogen evolution on supported incomplete cubane-type [Mo$_3$S$_4$]$^{4+}$ electrocatalysts.* The Journal of Physical Chemistry C, 2008. **112**(45): p. 17492-17498.

123. Zhang, Y.-Y., et al., *Fe/P dual doping boosts the activity and durability of* CoS_2 *polycrystalline nanowires for hydrogen evolution.* Journal of Materials Chemistry A, 2019. **7**(10): p. 5195-5200.

124. Li, Y., et al., *Ru single atoms and nanoclusters on highly porous N-doped carbon as a hydrogen evolution catalyst in alkaline solutions with ultrahigh mass activity and turnover frequency.* Journal of Materials Chemistry A, 2021. **9**(20): p. 12196-12202.

125. Wu, G., et al., *In-plane strain engineering in ultrathin noble metal nanosheets boosts the intrinsic electrocatalytic hydrogen evolution activity.* Nature Communications, 2022. **13**(1): p. 4200.

126. Li, H., et al., *Activating and optimizing* MoS_2 *basal planes for hydrogen evolution through the formation of strained sulfur vacancies.* Nature Materials, 2016. **15**(1): p. 48-53.

127. Wang, H., et al., *Electrochemical tuning of* MoS_2 *nanoparticles on three-dimensional substrate for efficient hydrogen evolution.* ACS Nano, 2014. **8**(5): p. 4940-4947.

128. Benck, J.D., et al., *Amorphous molybdenum sulfide catalysts for electrochemical hydrogen production: insights into the origin of their catalytic activity.* ACS Catalysis, 2012. **2**(9): p. 1916-1923.

129. Yin, Y., et al., *Contributions of phase, sulfur vacancies, and edges to the hydrogen evolution reaction catalytic activity of porous molybdenum disulfide nanosheets.* Journal of the American Chemical Society, 2016. **138**(25): p. 7965-7972.

130. Li, L., et al., *Role of sulfur vacancies and undercoordinated Mo regions in* MoS_2 *nanosheets toward the evolution of hydrogen.* ACS Nano, 2019. **13**(6): p. 6824-6834.

131. Tsai, C., et al., *Electrochemical generation of sulfur vacancies in the basal plane of* MoS_2 *for hydrogen evolution. Nat. Commun. 8, 15113.* 2017.

132. Seokhee, S., J. Zhenyu, B. Ranjith, and M. Yo-Sep, *High Turnover Frequency of Hydrogen Evolution Reaction on Amorphous* MoS_2 *Thin Film Directly Grown by Atomic Layer Deposition.* 2015.

133. Li, D.J., et al., *Molybdenum sulfide/N-doped CNT forest hybrid catalysts for high-performance hydrogen evolution reaction.* Nano letters, 2014. **14**(3): p. 1228-1233.

134. Chen, Z., et al., *Core-shell* MoO_3*–*MoS_2 *nanowires for hydrogen evolution: a functional design for electrocatalytic materials.* Nano letters, 2011. **11**(10): p. 4168-4175.